

# Electron-momentum dependence of electron-phonon coupling underlies dramatic phonon renormalization in $\text{YNi}_2\text{B}_2\text{C}$

Philipp Kurzthals<sup>1</sup>, Geoffroy Kremer<sup>2</sup>, Thomas Jaouen<sup>2,3</sup>, Christopher W. Nicholson<sup>2</sup>, Rolf Heid<sup>1</sup>, Peter Nagel<sup>1</sup>, John-Paul Castellan<sup>1,4</sup>, Alexandre Ivanov<sup>5</sup>, Matthias Muntwiler<sup>6</sup>, Maxime Rumo<sup>2</sup>, Bjoern Salzmänn<sup>2</sup>, Vladimir N. Strocov<sup>6</sup>, Dmitry Reznik<sup>7,8</sup>, Claude Monney<sup>2</sup>, Frank Weber<sup>1,✉</sup>

<sup>1</sup> Institute for Quantum Materials and Technologies, Karlsruhe Institute of Technology, 76021 Karlsruhe, Germany

<sup>2</sup> Département de Physique and Fribourg Center for Nanomaterials, Université de Fribourg, 1700 Fribourg, Switzerland

<sup>3</sup> Univ Rennes, CNRS, IPR (Institut de Physique de Rennes) - UMR 6251, F-35000 Rennes, France

<sup>4</sup> Laboratoire Léon Brillouin (CEA-CNRS), CEA Saclay, F-91191 Gif-sur-Yvette, France

<sup>5</sup> Institut Laue-Langevin, 71 avenue des Martyrs CS 20156, 38042 Grenoble Cedex 9, France

<sup>6</sup> Paul Scherrer Institut, Swiss Light Source, 5232 Villigen PSI, Switzerland

<sup>7</sup> Department of Physics, University of Colorado at Boulder, Boulder, Colorado 80309, USA

<sup>8</sup> Center for Experiments on Quantum Materials, University of Colorado at Boulder, Boulder, Colorado 80309, USA

✉ [frank.weber@kit.edu](mailto:frank.weber@kit.edu)

Electron-phonon coupling, i.e., the scattering of lattice vibrations by electrons and vice versa, is ubiquitous in solids and can lead to emergent ground states such as superconductivity and charge-density wave order. Strong coupling of phonons to electrons near the Fermi surface, which reduces the phonon lifetimes and broadens the phonon peaks in scattering experiments, is often associated with Fermi surface nesting. Here, we show that strong phonon broadening can occur in the absence of both Fermi surface nesting and lattice anharmonicity, if electron-phonon coupling is strongly enhanced for specific values of electron-momentum,  $\mathbf{k}$ . We use inelastic neutron scattering, soft x-ray angle-resolved photoemission spectroscopy measurements and *ab-initio* lattice dynamical and electronic band structure calculations to demonstrate this scenario in the highly anisotropic tetragonal electron-phonon superconductor  $\text{YNi}_2\text{B}_2\text{C}$ . This new scenario likely applies to a wide range of compounds.

## Introduction

Interacting degrees of freedom in solids underlie new emergent ground states and competing phases with potential for new functionalities. Vibrations of the atomic lattice, i.e. phonons, can couple to electrons<sup>1</sup>, magnetic<sup>2</sup>, or orbital degrees of freedom<sup>3</sup>. In particular, electron-phonon coupling (EPC) received a lot of attention as a microscopically understood origin of superconductivity. Furthermore, EPC has recently been in the focus of investigations of materials with competing phases such as cuprates<sup>4-8</sup> and layered transition-metal dichalcogenides<sup>9-13</sup>.

Reduced phonon lifetimes, are typically related to nesting where large sections of the Fermi surface (FS) are connected by a single phonon wave vector<sup>14-16</sup>. The hallmark of nesting is a singularity or at least strong peak in the electronic susceptibility for a particular phonon wave vector  $\mathbf{q}$  connecting parallel sections of the FS<sup>17,18</sup>.

Such phonon anomalies received a lot of attention recently in the context of charge density wave (CDW) formation, which is often driven by a soft phonon mode triggering a structural distortion at the CDW transition. In some CDW compounds, such as 1D conductors, this behavior is indeed related to the nesting of the FS<sup>19,20</sup>. Yet in others, such as  $2H$ -NbSe<sub>2</sub>, nesting is absent<sup>21-25</sup> and cannot explain the soft-mode properties. While the CDW in  $2H$ -NbSe<sub>2</sub> originates from EPC<sup>21,26</sup>, it has been proposed that the phonon softening and broadening on cooling towards the CDW transition temperature  $T_{CDW}$  can be explained only by taking into account lattice fluctuations<sup>24</sup>, and anharmonic effects may play an important role<sup>23</sup>. Phonon anomalies in cuprates remain enigmatic though a strong response to the onset of superconductivity is evident<sup>4,7</sup>. In other cases, an expected phonon broadening related to nesting is absent<sup>27</sup> or incomplete<sup>28</sup>. In principle, the phonon momentum,  $\mathbf{q}$ , dependence of the EPC itself, expressed in the EPC matrix elements  $g_{\vec{k}+\vec{q},\vec{k}}^{\vec{q}\lambda}$ , can determine the wavevector of the phonon broadening in the absence of FS nesting<sup>25,26</sup>. Yet,  $g_{\vec{k}+\vec{q},\vec{k}}^{\vec{q}\lambda}$  is expected to be temperature-independent for temperatures of the order of up to  $10^3$  K.

Here, we propose a scenario in which the electron momentum,  $\mathbf{k}$ , dependence of the EPC matrix elements comes into play. In such a scenario, the  $g_{\vec{k}+\vec{q},\vec{k}}^{\vec{q}\lambda}$ , is particularly large for electrons on certain parts of the FS. We show that such  $\mathbf{k}$ -selective EPC can be strong enough to significantly broaden phonons even when  $\mathbf{k}$ -integrated quantities like the electronic susceptibility  $\chi_q$  lack particular features at the phonon momentum  $\mathbf{q}$ . In this case, the broadening can sensitively depend on the temperature-induced changes of electronic states at the Fermi energy. This scenario can explain large temperature-dependent phonon linewidths in the absence of both nesting and anharmonicity.

We demonstrate this scenario on the electron-phonon superconductor YNi<sub>2</sub>B<sub>2</sub>C ( $T_c = 15.2$  K). YNi<sub>2</sub>B<sub>2</sub>C is known for unusual low-temperature phonon line shapes reflecting the anisotropic superconducting energy gap<sup>29-31</sup>, EPC distributed over 160 meV in phonon energy<sup>32</sup> and phonons with unusual eigenvectors mediating superconductivity<sup>33</sup>. This work focuses on the microscopic origin of strongly increased linewidths of certain phonons observed over a large range of wavevectors in the normal state at low temperatures, i.e.  $T = 20$  K.

We first argue that previously proposed explanations for the phonon properties in YNi<sub>2</sub>B<sub>2</sub>C, i.e., FS nesting<sup>34</sup>, can be ruled out. Then we demonstrate that results of our comprehensive inelastic neutron scattering (INS) and soft x-ray angle-resolved photoemission spectroscopy (SX-ARPES) measurements agree well with *ab-initio* lattice dynamical and electronic band structure calculations, which allows us to use these calculations to gain insights into the microscopic origin of EPC. The calculations highlight the importance of 2D electronic joint density of states

(2D-eJDOS). It is defined as the usual electronic joint density of states (eJDOS) but evaluated for 2D slices of the reciprocal space at a specific component of  $\mathbf{k}$ ,  $k_z$ , where the z-direction is defined to be parallel to the crystallographic  $c$  axis (Fig. 1a,b). The results highlight the decisive role of the interplay between the  $\mathbf{k}$ -dependence of the EPC combined with a strongly  $\mathbf{k}$ -dependent 2D-eJDOS, and explain strongly temperature-dependent phonon broadening in the absence of FS nesting and lattice anharmonicity.

## Background

### ***Effect of electron-phonon coupling on phonons***

Electron-phonon coupling renormalizes phonon energies and reduces the phonon lifetime through phonon emission or absorption by electron-hole pairs. Quantitatively, phonon energy is affected by the real part of the  $\mathbf{q}$  dependent electronic susceptibility  $\chi_{\mathbf{q}}$ , whereas the lifetime is determined by the imaginary part [see Feynman diagram in Fig. 1(a)]. The former depends on electronic states near as well as far from the Fermi surface, whereas only electronic states near the FS contribute to the latter.

Thus knowledge of both electrons and phonons as well as the coupling between them is necessary to understand phonon self-energy in metals. It is easier to compare theory with experiments for the phonon lifetimes than for the peak positions, because electronic states near the FS can be accurately measured by Angle Resolved Photoemission (ARPES) and the phonon linewidths can be measured by neutron scattering. On the other hand, measurements of electronic states far from the FS that need to be included to obtain phonon peak shift due to interaction with electrons are a lot more challenging especially for the states that are unoccupied.

Phonon lifetimes are reduced when electrons are excited to energies larger than  $E_F$  by phonon absorption and relax by phonon emission. Since the energy and momentum are conserved, only occupied electronic states in a small energy window  $E_F - E_{phon}^{q\lambda}$  can contribute to this process, where  $E_{phon}^{q\lambda}$  is the energy of a phonon mode with wave vector  $\mathbf{q}$  in the dispersion branch  $\lambda$  [Fig. 1(b)]. Reduced lifetimes translate into large line widths of phonon scattering spectra.

Two quantities are relevant for determining phonon line broadening due to the EPC: (1) The likelihood that a particular phonon with  $E_{phon}^{q\lambda}$  is scattered/absorbed by a particular electron in a state with wave vector  $\mathbf{k}$  and energy  $E_{el}^k$ , which is expressed as the EPC matrix element  $g_{\vec{k}+\vec{q},\vec{k}}^{\vec{q}\lambda}$ . (2) The imaginary part of the electronic susceptibility  $\chi_{\mathbf{q}}''$  reflects the number of electronic states at the FS which are connected by  $\mathbf{q}$ , i.e. the eJDOS, which is defined as  $\sum_{\vec{k}} \delta(E_{\vec{k}} - E_F) \delta(E_{\vec{k}+\vec{q}} - E_F)$  and equivalent to the so-called nesting function  $\xi(\mathbf{q})$ <sup>35,a</sup>. Both  $g_{\vec{k}+\vec{q},\vec{k}}^{\vec{q}\lambda}$  and  $\chi_{\mathbf{q}}$  are in general  $\mathbf{q}$  dependent and, therefore, their interplay in  $\mathbf{q}$ -space determines the  $\mathbf{q}$ -dependence of phonon linewidths [Fig. 1(c)]. Equation (1) describes the contribution  $\gamma_{EPC}^{\mathbf{q}}$  to the phonon linewidth  $\Gamma \propto (\text{phonon lifetime})^{-1}$  because of EPC:

$$\gamma_{EPC}^{\mathbf{q}} = \pi\omega_{q\lambda} \sum_{\vec{k}} \left| g_{\vec{k}+\vec{q},\vec{k}}^{\vec{q}\lambda} \right|^2 \delta(\epsilon_{\vec{k}} - \epsilon_F) \delta(\epsilon_{\vec{k}+\vec{q}} - \epsilon_F) \quad (1)$$

<sup>a</sup> In the following, we will use the term eJDOS. The equivalent term *nesting function* could cause confusion since conventional FS nesting plays absolutely no role in the reported effects.

Apart from their intrinsic  $\mathbf{q}$  dependence, the EPC matrix elements  $g_{\mathbf{k}+\bar{\mathbf{q}},\bar{\mathbf{k}}}^{q\lambda}$  can amplify or suppress contributions to the phonon linewidth for electronic states at different  $\mathbf{k}$ . This  $\mathbf{k}$ -selectivity has not yet been considered in the analysis of EPC. We show that it can have a profound impact on the lattice dynamical properties as exemplified by the behavior of the phonon broadening in YNi<sub>2</sub>B<sub>2</sub>C.

### **Lattice dynamics in YNi<sub>2</sub>B<sub>2</sub>C**

YNi<sub>2</sub>B<sub>2</sub>C offers unique insights into the interplay between electronic and lattice degrees of freedom via superconductivity-induced phonon anomalies<sup>29,31,36</sup>. Phase competition of superconductivity with CDW order<sup>34</sup>, the role of FS nesting<sup>37-39</sup> as well as its lattice dynamics have been investigated extensively<sup>29,40</sup> including in our earlier work<sup>31-33</sup>. We first demonstrate that temperature and  $\mathbf{q}$  dependence of phonon renormalization in YNi<sub>2</sub>B<sub>2</sub>C is inconsistent with either standard mechanism: FS nesting or anharmonicity.

Overall, *ab-initio* lattice dynamical calculations of YNi<sub>2</sub>B<sub>2</sub>C agree with phonon spectroscopy results at energies up to 160 meV with regard to both phonon energies and corresponding phonon linewidths due to the EPC<sup>31-33</sup>. The strongest phonon anomalies are observed in *c*-axis polarized transverse acoustic (TA) phonon modes<sup>33</sup>. One such mode at  $\mathbf{q} = (0.5, 0.5, 0)$ , the *M* point of the Brillouin zone (BZ), is measured at  $\mathbf{Q} = (0.5, 0.5, 7)$ , i.e., in the BZ adjacent to  $\boldsymbol{\tau} = (1, 0, 7)$  [Fig. 2(a)]. Another strong coupling TA mode is observed at  $\mathbf{q} = (0.55, 0, 0)$ , i.e., about half-way between the  $\Gamma$  and *X* = (1, 0, 0) points of the BZ. For simplicity, we call it here the *X/2* anomaly. We measured it at  $\mathbf{Q} = (0.45, 0, 7)$ , i.e. close to the same BZ center as the *M* point phonon, i.e.  $\boldsymbol{\tau} = (1, 0, 7)$  [Fig. 2(b)]. The *X/2* anomaly is the only part of the phonon dispersion, which is not very well captured by *ab-initio* calculations in that the observed anomaly is stronger than predicted<sup>33</sup>.

Key enigmatic results are (1) that strong phonon broadening is observed over a wide range of phonon wave vectors  $\mathbf{q} = (h, 0, 0)$ ,  $0.4 \leq h \leq 0.75$ , i.e.  $\mathbf{q} \approx X/2$ , but quickly vanishes going away from  $\mathbf{q} = (0.5, 0.5, 0)$  along the [110] direction and (2) that broadening of the TA mode at *X/2* is much stronger than at the *M* point. Both TA phonons display a pronounced broadening upon cooling from room temperature to  $T = 20$  K easily identified in high energy resolution INS data (see methods) [Figs. 2(a)(b)]. The new data allows for a detailed study of the momentum dependence of phonon broadening (see Results section and Figs. 5, S7-S9).

The observed broadening at  $\mathbf{q} \approx X/2$  is much stronger than at the *M* point [Figs. 2(a)(b)]. In contrast, the calculated eJDOS<sup>33</sup> along the [100] and [110] directions displays a peak only for  $\mathbf{q} = (0.5, 0.5, 0)$  [Fig. 2(c)]. Yet, the calculations correctly predict the broad momentum range along the [100] direction over which phonon broadening is observed<sup>33</sup>. Therefore, nesting is unlikely to be the origin of the observed strong phonon renormalization. On the other hand, EPC matrix elements  $g_{\mathbf{k}+\bar{\mathbf{q}},\bar{\mathbf{k}}}^{q\lambda}$  [see Eq. (1)] can underlie a  $\mathbf{q}$  dependence not reflected by the FS geometry. However, the matrix elements are expected to change only for temperatures on the order of an *electron-volt* corresponding to much higher values than those in Figure 2.

Anharmonic broadening of phonons is typically attributed to phonon-phonon scattering which is typically strong at elevated temperatures.<sup>41,42</sup> At low temperatures anharmonic broadening can occur near or at structural phase transitions as it is argued for the case of the CDW transition in 2H-NbSe<sub>2</sub> ( $T_{\text{CDW}} = 33$  K).<sup>23</sup> In fact, it was argued that YNi<sub>2</sub>B<sub>2</sub>C is close to a structural phase transition related to the soft mode at  $\mathbf{q} \approx (0.5, 0, 0)$  only precluded by the onset of superconductivity.<sup>34</sup> Hence, the large phonon linewidth just above  $T_c = 15.2$  K could still be anharmonic. However, previously reported superconductivity-induced changes of the line shape of the anomalous

TA phonons rule out a non-electronic origin.<sup>29</sup> This redistribution of phonon spectral weight<sup>31</sup> directly reflects the opening of the superconducting gap  $2\Delta$  (for more details see Fig. S1 and Supplementary Note 1). A model<sup>36</sup> which accurately describes these observations is purely EPC-based, which is possible only if phonon broadening in  $\text{YNi}_2\text{B}_2\text{C}$  occurs only related to electronic scattering, i.e., is EPC in nature.

In the following we present evidence that the strong TA phonon broadening in  $\text{YNi}_2\text{B}_2\text{C}$  originates from EPC that is strongly enhanced on parts of the Fermi surface, which are connected by the correct values of the phonon momentum. This scenario explains the results from phonon spectroscopy [see Figs. 2(a)(b)] in the absence of FS nesting or lattice anharmonicity.

## Results

### **Band structure from electron spectroscopy**

There has been considerable discussion about FS nesting for  $q \approx X/2$  in  $(\text{Lu}/\text{Y})\text{Ni}_2\text{B}_2\text{C}$  including theoretical<sup>34,37,43</sup> and experimental work<sup>38,39,44,45</sup>. Yet, the clearest signature of electron phonon coupling, the  $T_c$ -induced phonon effect, appears over a large momentum region along the [100] direction<sup>31</sup>, which is inconsistent with nesting. In order to clarify the origin of this EPC, we performed SX-ARPES measurements on samples cut from the large  $\text{YNi}_2\text{B}_2\text{C}$  single crystal, which we used for our current and also previous INS studies<sup>31-33</sup>.

SX-ARPES measurements at photon energies  $h\nu \geq 650$  eV have a resolution, which is sharp enough to reliably resolve the  $k_z$ -dispersion effects in  $\text{YNi}_2\text{B}_2\text{C}$ .<sup>b</sup> We compared the experimentally observed band structure with density functional theory (DFT) calculations carried out in the framework of the mixed basis pseudopotential method<sup>46</sup> using the local density approximation (LDA) (for details see<sup>33</sup>).

Selected cuts of the FS in the  $k_x - k_y$  plane in Figs. 3(a)-(c) and the  $k_x - k_z$  plane in Fig. 3(d)(e) overlaid with corresponding DFT calculations (solid blue lines), show a good agreement (see also Figs. S2 and S3 in SI). We focus on the vicinity of the  $M$  point, i.e. at  $\mathbf{k} = (0.5, 0.5, k_z)$ , since the DFT predicts a square shaped FS around it for certain  $k_z$  values prone to nesting<sup>33</sup>. Our results demonstrate the significant evolution of the FS at  $M$ : An elliptical FS stretches between the four visible  $\Gamma$  points at  $k_z = 23$  r.l.u. [Fig. 3(a),  $h\nu = 693$  eV], a nearly square-shaped feature is found at  $k_z = 23.5$  r.l.u. [Fig. 3(b),  $h\nu = 725$  eV], and a large nearly circular ellipse is observed at  $k_z = 24$  r.l.u. [Fig. 3(c),  $h\nu = 758$  eV] with the long axis rotated by  $90^\circ$  relative to the orientation at  $k_z = 23$  r.l.u.. Note that due to the particular symmetry of the BZ, the positions of  $\Gamma$  and  $Z$  points are reversed upon moving from  $k_z = 23$  r.l.u. to  $k_z = 24$  r.l.u. [see Fig. 3(f)].

The experimentally observed spectral weight with a square-like shape for  $k_z = 23.5$  r.l.u. is relatively diffuse, in contrast to the sharp FS expected from the calculated Fermi contour [Fig. 3(b)]. This originates from two features of the band structure in the vicinity of the  $M$  point: (1) The  $k_z$  dispersion of the inner band is very strong [Fig. 3(d)(e) and Fig. S4(c)] and (2) both the inner and outer bands forming the square have a shallow in-plane energy dispersion of less than 0.5 eV near  $E_F$  [see Fig. S3(c)]. Hence, due to the uncertainty of the inner potential  $V_0$  used in rendering photon energy into  $k_z$  and to the limited  $k_z$  and energy resolution of the experiment, we pick up intensity inside the square.

<sup>b</sup> The half out-of-plane periodicity of the BZ, i.e. the  $\Gamma - Z$  distance [see Fig. 3(f)], is  $2\pi/c = 0.597 \text{ \AA}^{-1}$  [ $k_z = 1$  r.l.u.], which corresponds to a difference in the incident photon energy of  $\Delta(h\nu) \approx 65$  eV.

We used both linear vertical, i.e.  $p$ , and linear horizontal, i.e.  $s$  polarization of the light in order to exploit photoemission matrix element effects.  $p$  polarization is sensitive to the inner (outer) band for odd (even) values of  $k_z$ , whereas  $s$  polarization reveals inner and outer bands for both odd and even  $k_z$ . This is evident in Figures 3(a)(c) where the spectral weight is located at the center and at the edges of the ellipse at the  $M$  point, respectively, with  $p$ , but uniformly distributed with  $s$  [bottom right in Fig. 3(a)]. This is also visible on the  $k_z$  dispersion for  $k_z = 0.5$  r.l.u. [Figs. 3(d)(e)]. With  $p$  polarization [Fig. 3(d)], the experimental periodicity of the band structure looks like it is doubled in comparison to the calculations due to these matrix elements effects. In fact, we recover the correct periodicity using  $s$  polarization of the light [Fig. 3(e)]. Note that the data of Figure 3(d) cut the  $M$  point in the  $k_x - k_y$  plane between the first and second BZ, while the data of Figure 3(e) cut the  $M$  point between the second and third BZ. However, Figures 3(a)-(c) indicate that variations of the photoemission matrix elements across different BZs are smaller than variations due to light polarization.

### **Electronic joint density of states from density functional theory**

The SX-ARPES study detailed above shows that the band structure of  $\text{YNi}_2\text{B}_2\text{C}$  is well described by our DFT calculations. Therefore, we rely on the analysis of the calculated FS (see Fig. S4) to assess the nesting properties of  $\text{YNi}_2\text{B}_2\text{C}$  via the calculated eJDOS. The eJDOS along the [100] and [110] directions in  $\mathbf{q}$  [Figs. 2(c) and 4(a)] lacks a peak at the position of the most pronounced  $\mathbf{q} \approx X/2$  phonon broadening. However, our calculations reveal a peculiar momentum dependence when we look at the joint electronic density of states analyzed for fixed values of  $k_z$ , which we call a 2D-eJDOS. Detailed  $k_z$ -dependent calculations for phonon wave vectors  $\mathbf{q}$  in the entire  $[h, k, 0]$  plane reveal that the 2D-eJDOS is low for  $k_z = 0$  [Fig. 4(b)] but increases strongly to  $k_z = 0.5$  r.l.u. [Fig. 4(c) and Figs. S5 and S6].

We report the  $k_z$  dependence of the 2D-eJDOS in more detail for three  $\mathbf{q}$  ranges defined in Figure 4(b): (1)  $\mathbf{q} = (h, k, 0)$  with  $0 \leq h, k \leq 1$  [large blue square], (2)  $\mathbf{q} \approx X/2$  [red bar] and (3)  $\mathbf{q} \approx M$  [green bar]. Starting with range (1), the corresponding  $\mathbf{q}$ -averaged 2D-eJDOS,  $\overline{2D - eJDOS}_q$ , has a clear peak at  $k_z = 0.5$  r.l.u. [Fig. 4(d)]. Corresponding data for ranges (2)  $\mathbf{q} = X/2$  [Fig. 4(e)] and (3)  $\mathbf{q} = M$  [Fig. 4(f)] show that the peak of the  $\overline{2D - eJDOS}_q$  at  $k_z = 0.5$  r.l.u. is even more pronounced at the wave vectors of the strong phonon broadening. Overall, our analysis demonstrates that the 2D-eJDOS is extremely sensitive to  $k_z$  and depends less on the phonon wave vector  $\mathbf{q}$ .

### **Momentum-dependent phonon broadening from inelastic neutron scattering**

So far, we focused on the mechanism explaining the strong broadening of the two TA modes at  $\mathbf{q} \approx X/2$  and  $\mathbf{q} = M$  [Figs. 2(a)(b)]. While these effects are not sharply localized in  $\mathbf{q}$  space, they do depend on the phonon wave vector<sup>33</sup> and only a rigorous experimental test enables an overall verification of the validity of the DFT calculations. Therefore, we performed neutron scattering experiments with improved energy resolution at phonon wave vectors along as well as off the high-symmetry directions investigated previously<sup>29,31,33</sup>. We compare our results to *ab-initio* calculations of  $\gamma_{EPC}^q$  (see Eq. 1), which were calculated using the linear response technique or density functional perturbation theory (DFPT)<sup>47</sup> in combination with the mixed-basis pseudopotential method<sup>48</sup>.

For the present study, we measured phonons at wave vectors close to  $\mathbf{q} = X/2$  and the  $M$  point at room temperature and  $T = 20$  K and looked for peak broadening. We observed broad but clear momentum

dependences, e.g., in measurements going away from the  $M$  point [see Fig. 2(a)]: Already at close-by wavevectors, the broadening is clearly reduced [Fig. 5(a)] and completely absent further away in momentum space [Fig. 5(b)]. More INS data taken along different directions for both anomalous modes are shown in Figure S7 of SI. The experimentally observed  $\mathbf{q}$  dependence of phonon broadening [symbols in Fig. 5(c)] is in good agreement with the calculated one of  $\gamma_{EPC}^q$  [color code in Fig. 5(c)]. Similar agreement is found for phonon wavevectors with a non-zero  $l$  component (Figs. S8 and S9 and Supplementary Note 2).

Finally, we note that the  $\mathbf{k}$ -averaged eJDOS is about 50% higher for the  $M$  point than for  $\mathbf{q} \approx X/2$  [Fig. 2(c) and 4(a)], whereas the  $\overline{2D - e}JDOS_q(k_z = 0.5 \text{ r.l.u.})$  [Figs. 4(c),(e)(f) and Fig. S6] and  $\gamma_{EPC}^q$  [Fig. 5(c)] have similar values at these two wave vectors. This is further evidence that the electronic states at the Fermi level with  $k_z = 0.5 \text{ r.l.u.}$  are selected by EPC matrix elements and mediate the coupling responsible for the broadening of the TA phonons in  $\text{YNi}_2\text{B}_2\text{C}$ .

## Discussion

EPC has been studied for a long time because it can stabilize emergent ground states as well as lead to phase competition. The particular role/impact of EPC matrix elements was discussed already in the 1970s,<sup>49,50</sup> though experimental evidence for the decisive role of the momentum dependence of the EPC matrix elements was only reported in the last decade<sup>23,25,26,51-53</sup>. Still, only the  $\mathbf{q}$  dependence of the EPC matrix element  $g_{\vec{k}+\vec{q},\vec{k}}^{\vec{q}\lambda}$  was scrutinized. Our work takes the full  $\mathbf{k}$  and  $\mathbf{q}$  momentum dependence of  $g_{\vec{k}+\vec{q},\vec{k}}^{\vec{q}\lambda}$  into account. We can explain not only phonon broadening due to EPC as a function of  $\mathbf{q}$  but also its pronounced weakening at increased temperatures in the absence of FS nesting and anharmonicity. The peak of the  $\overline{2D - e}JDOS_q$  as function of  $k_z$  [Figs. 4(d)-(f)] accounts for a high sensitivity to temperature via the electronic band structure if the contribution of the electronic states with  $k_z = 0.5 \text{ r.l.u.}$  to EPC is boosted by  $\mathbf{k}$ -selective matrix elements. The peak of the  $\overline{2D - e}JDOS_q(k_z)$  [Figs. 4(d)-(f)] is superficially reminiscent of classic FS nesting scenario where the peak in the  $\mathbf{k}$ -averaged eJDOS( $\mathbf{q}$ ) associated with the nesting condition is responsible for a phonon anomaly. At increased temperatures, smearing of the Fermi function quickly suppresses this peak in the eJDOS( $\mathbf{q}$ ) and reduces the phonon broadening.<sup>18</sup> In our case, the peaks in the  $\overline{2D - e}JDOS_q(k_z)$  [Figs. 4(d)-(f)] are expected to also be strongly broadened and reduced in height with increasing temperatures. This is exactly what is observed in experiments. Our results demonstrate that  $\mathbf{k}$  selectivity of the EPC can boost the contribution of only a small part of the Fermi surface to the phonon lifetime. This new point of view has to be taken into account generally when assessing phonon anomalies in metallic systems.

This finding makes it necessary to reconsider our understanding of some well-known materials.  $\text{NbSe}_2$  is a model system for various fundamental aspects (phase competition as function of dimensionality<sup>12</sup>; quantum phase transitions<sup>54,55</sup>; 2D quantum metal state<sup>56</sup>; Higgs mode in condensed matter physics<sup>57,58</sup>). The correct view of EPC is indispensable ingredient for explaining many of the observed effects. In particular,  $\text{NbSe}_2$  is considered to be a showcase for  $\mathbf{q}$ -dependent EPC matrix elements featuring concomitant charge-density-wave (CDW) order ( $T_{CDW} = 33 \text{ K}$ ) and phonon-mediated superconductivity ( $T_c = 7.2 \text{ K}$ )<sup>59</sup>. Calculations<sup>24</sup> and experiments<sup>25</sup> have shown that FS nesting is absent and concluded that the periodicity of the CDW is determined by the momentum dependence of the EPC matrix elements. Thus, the phonon broadening and softening close to  $T_{CDW}$  is due to the EPC. However, lattice fluctuations overwhelm EPC away from  $T_{CDW}$  and explain the strongly reduced phonon renormalization at

elevated temperatures<sup>23,24</sup>. We find that the calculated eJDOS across the CDW ordering wavevector  $\mathbf{q}_{CDW}$  in  $2H$ -NbSe<sub>2</sub> is nearly featureless whereas the calculated linewidth due to EPC,  $\gamma_{EPC}^q$ , shows a pronounced broad maximum around  $\mathbf{q}_{CDW}$  in agreement with experiment<sup>26</sup>. The situation is, in fact, very similar to that observed for the  $X/2$  anomaly in YNi<sub>2</sub>B<sub>2</sub>C [see Figs. 2(c) and 5(c)]. In analogy to the results presented here, the strong temperature dependence of the phonon linewidth in  $2H$ -NbSe<sub>2</sub> could also originate from an interplay of  $\mathbf{k}$ -selective EPC and the electronic band structure. In fact, Flicker *et al.*<sup>24</sup> already considered an orbital-dependent EPC matrix element. Yet, it remains unclear whether the model calculations also support a strongly  $\mathbf{k}$  dependent 2D-eJDOS. Recently, phonon anomalies related to CDW order in cuprates have attracted large scientific interest. In particular, a strong phonon broadening was observed at and below the onset of CDW fluctuations competing with superconductivity<sup>4,8,6</sup>. The abrupt decrease of the phonon linewidth in YBa<sub>2</sub>Cu<sub>3</sub>O<sub>6.6</sub> on entering the superconducting state<sup>4</sup> indicates a high-sensitivity to the opening of the superconducting energy gap on the FS mediated by the EPC. Yet, the mechanism determining the periodicity of the CDW remains unclear. The reported sharp  $\mathbf{q}$  dependence of the phonon broadening is reminiscent of a FS nesting-type origin but the nesting could not be identified in the electronic band structure.  $\mathbf{k}$  selective EPC in concert with large 2D-eJDOS on a small part of the FS is a novel approach for an improved understanding of these observations.

## Materials and Methods

**Inelastic neutron scattering** experiments were performed at the  $1T$  and  $IN8$  triple-axis spectrometers located at Laboratoire Léon Brillouin (LLB), CEA Saclay, and Institute Laue-Langevin (ILL), Grenoble, respectively. Double focusing pyrolytic graphite monochromators and analyzers were employed on the  $1T$  spectrometer. We used double focusing copper (Cu200) monochromators and analyzers on  $IN8$ . A fixed analyzer energy of 14.7 meV allowed us to use a graphite filter in the scattered beam to suppress higher orders. The phonon scattering wave vector  $\mathbf{Q} = \boldsymbol{\tau} + \mathbf{q}$  is expressed in reciprocal lattice units (r.l.u.)  $(2\pi/a, 2\pi/b, 2\pi/c)$  with the lattice constants  $a = b = 3.51 \text{ \AA}$  and  $c = 10.53 \text{ \AA}$  of the tetragonal unit cell. The single crystal sample was mounted in a standard orange cryostat at ILL and in a closed-cycle refrigerator at LLB, allowing measurements down to  $T = 2 \text{ K}$ .

**Soft x-ray angle resolved photoemission spectroscopy** experiments were performed on in-situ cleaved single crystals of YNi<sub>2</sub>B<sub>2</sub>C (001 surface) at the SX-ARPES endstation<sup>60</sup> at ADRESS beamline<sup>61</sup> of the Swiss Light Source (SLS) with incident photon energies  $h\nu$  in the range 680 – 900 eV (for more details see<sup>60</sup>). The increase of the photoelectron mean-free path related to the increased kinetic energy in the soft x-ray regime translates into a proportional improvement of the intrinsic  $k_z$  resolution of the photoemission experiment, which is indispensable for our investigation. The measurements were performed at low sample temperature  $T = 20 \text{ K}$  in order to suppress relaxation of  $\mathbf{k}$ -selectivity because of thermal motion<sup>62</sup>. For consistency with the results from neutron scattering, the electron scattering wave vector  $\mathbf{k}$  is expressed in r.l.u.  $(2\pi/a, 2\pi/b, 2\pi/c)$ .

**Density functional theory** calculations were carried out in the framework of the mixed basis pseudopotential method<sup>46</sup> using the local density approximation (LDA) (for details see<sup>33</sup>) with a  $80 \times 80 \times 30$  grid of points in  $\mathbf{k}$  space. Plots of the electronic band structure and its properties are based on an interpolated  $200 \times 200 \times 30$  grid to enhance the in-plane accuracy. All results presented here were obtained for the experimental lattice constants of the tetragonal structure ( $a = b = 3.51 \text{ \AA}$ ,  $c = 10.53 \text{ \AA}$ ) with internally relaxed atomic coordinates. Phonon properties and EPC matrices were calculated for a  $32 \times 32 \times 16$  grid in phonon, i.e.  $\mathbf{q}$  momentum space using the

linear response technique or density functional perturbation theory (DFPT)<sup>47</sup> in combination with the mixed-basis pseudopotential method<sup>48</sup>.

## Acknowledgments

We acknowledge local support from Daria Sostina during test experiments at the PEARL beamline at SLS. This project was supported from the Swiss National Science Foundation (SNSF) Grant No. P00P2\_170597. We acknowledge the Paul Scherrer Institute, Villigen, Switzerland for provision of synchrotron radiation beamtime at beamline ADRESS of the Swiss Light Source. D.R. was supported by the DOE, Office of Basic Energy Sciences, Office of Science, under Contract No. DE-SC0006939.

## AUTHOR CONTRIBUTIONS

Neutron scattering: P.K., J.-P.C., A.I., D.R., F.W.; photo-emission spectroscopy: G.K., C.N., P.K., M.R., B.S., T.J., V.S., P.N., C.M., F.W.; theory: R.H., P.K., F.W.; data analysis: P.K., G.K., C.M., F.W.; manuscript: G.K., C.N., T.J., D.R., C.M., F.W.

## ADDITIONAL INFORMATION

Supplementary Information accompanies this paper.

## References

- 1 Errea, I., Calandra, M., Pickard, C. J., Nelson, J. R., Needs, R. J., Li, Y., Liu, H., Zhang, Y., Ma, Y. & Mauri, F. Quantum hydrogen-bond symmetrization in the superconducting hydrogen sulfide system. *Nature* **532**, 81-84 (2016).
- 2 Krannich, S., Sidis, Y., Lamago, D., Heid, R., Mignot, J. M., Lohneysen, H. v., Ivanov, A., Steffens, P., Keller, T., Wang, L., Goering, E. & Weber, F. Magnetic moments induce strong phonon renormalization in FeSi. *Nat Commun* **6**, 8961 (2015).
- 3 Weber, F., Aliouane, N., Zheng, H., Mitchell, J. F., Argyriou, D. N. & Reznik, D. Signature of checkerboard fluctuations in the phonon spectra of a possible polaronic metal  $\text{La}_{1.2}\text{Sr}_{1.8}\text{Mn}_2\text{O}_7$ . *Nature materials* **8**, 798-802 (2009).
- 4 Le Tacon, M., Bosak, A., Souliou, S. M., Dellea, G., Loew, T., Heid, R., Bohnen, K. P., Ghiringhelli, G., Krisch, M. & Keimer, B. Inelastic X-ray scattering in  $\text{YBa}_2\text{Cu}_3\text{O}_{6.6}$  reveals giant phonon anomalies and elastic central peak due to charge-density-wave formation. *Nature Physics* **10**, 52-58 (2014).
- 5 Blanco-Canosa, S., Frano, A., Schierle, E., Porras, J., Loew, T., Minola, M., Bluschke, M., Weschke, E., Keimer, B. & Le Tacon, M. Resonant x-ray scattering study of charge-density wave correlations in  $\text{YBa}_2\text{Cu}_3\text{O}_{6+x}$ . *Physical Review B* **90**, 054513 (2014).
- 6 Miao, H., Ishikawa, D., Heid, R., Le Tacon, M., Fabbris, G., Meyers, D., Gu, G. D., Baron, A. Q. R. & Dean, M. P. M. Incommensurate Phonon Anomaly and the Nature of Charge Density Waves in Cuprates. *Physical Review X* **8**, 011008 (2018).
- 7 Kim, H.-H., Souliou, S. M., Barber, M. E., Lefrançois, E., Minola, M., Tortora, M., Heid, R., Nandi, N., Borzi, R. A., Garbarino, G., Bosak, A., Porras, J., Loew, T., König, M., Moll, P. J. W., Mackenzie, A. P., Keimer, B., Hicks, C. W. & Le Tacon, M. Uniaxial pressure control of competing orders in a high-temperature superconductor. *Science* **362**, 1040-1044 (2018).
- 8 Blackburn, E., Chang, J., Said, A. H., Leu, B. M., Liang, R., Bonn, D. A., Hardy, W. N., Forgan, E. M. & Hayden, S. M. Inelastic x-ray study of phonon broadening and charge-density wave formation in ortho-II-ordered  $\text{YBa}_2\text{Cu}_3\text{O}_{6.54}$ . *Physical Review B* **88**, 054506 (2013).
- 9 Sipos, B., Kuzmartseva, A. F., Akrap, A., Berger, H., Forró, L. & Tutiš, E. From Mott state to superconductivity in 1T-TaS<sub>2</sub>. *Nature materials* **7**, 960-965 (2008).
- 10 Kuzmartseva, A., Sipos, B., Berger, H., Forró, L. & Tutiš, E. Pressure Induced Superconductivity in Pristine 1T-TiSe<sub>2</sub>. *Physical Review Letters* **103**, 236401 (2009).
- 11 Joe, Y. I., Chen, X. M., Ghaemi, P., Finkelstein, K. D., de la Pena, G. A., Gan, Y., Lee, J. C. T., Yuan, S., Geck, J., MacDougall, G. J., Chiang, T. C., Cooper, S. L., Fradkin, E. & Abbamonte, P. Emergence of charge density wave domain walls above the superconducting dome in 1T-TiSe<sub>2</sub>. *Nature Physics* **10**, 421-425 (2014).
- 12 Xi, X., Zhao, L., Wang, Z., Berger, H., Forró, L., Shan, J. & Mak, K. F. Strongly enhanced charge-density-wave order in monolayer NbSe<sub>2</sub>. *Nature Nanotechnology* **10**, 765-769 (2015).

- 13 Yang, H., Kim, S. W., Chhowalla, M. & Lee, Y. H. Structural and quantum-state phase transition in van der Waals layered materials. *Nature Physics* **13**, 931 (2017).
- 14 Renker, B., Rietschel, H., Pintschovius, L., Gläser, W., Brüesch, P., Kuse, D. & Rice, M. J. Observation of Giant Kohn Anomaly in the One-Dimensional Conductor  $\text{K}_2\text{Pt}(\text{CN})_4\text{Br}_{0.3}\cdot 3\text{H}_2\text{O}$ . *Physical Review Letters* **30**, 1144 (1973).
- 15 Hoesch, M., Bosak, A., Chernyshov, D., Berger, H. & Krisch, M. Giant Kohn Anomaly and the Phase Transition in Charge Density Wave  $\text{ZrTe}_3$ . *Physical Review Letters* **102**, 086402 (2009).
- 16 Hoesch, M., Cui, X., Shimada, K., Battaglia, C., Fujimori, S.-i. & Berger, H. Splitting in the Fermi surface of  $\text{ZrTe}_3$ : A surface charge density wave system. *Physical Review B* **80**, 075423 (2009).
- 17 Bohnen, K., Heid, R., Liu, H. J. & Chan, C. T. Lattice Dynamics and Electron-Phonon Interaction in (3,3) Carbon Nanotubes. *Physical Review Letters* **93**, 245501 (2004).
- 18 Johannes, M. D. & Mazin, I. I. Fermi surface nesting and the origin of charge density waves in metals. *Physical Review B* **77**, 165135 (2008).
- 19 Comes, R., Renker, B., Pintschovius, L., Currat, R., Glaser, W. & Scheiber, G. Inelastic Neutron-Scattering Study of  $2k_F$  Instability in  $\text{K}_2\text{Pt}(\text{CN})_4\text{Br}_{0.3}\cdot 3\text{D}_2\text{O}$ . *Physica Status Solidi B-Basic Research* **71**, 171-178 (1975).
- 20 Grüner, G. The dynamics of charge-density waves. *Reviews of Modern Physics* **60**, 1129-1181 (1988).
- 21 Johannes, M. D., Mazin, I. I. & Howells, C. A. Fermi-surface nesting and the origin of the charge-density wave in  $\text{NbSe}_2$ . *Physical Review B* **73**, 205102 (2006).
- 22 Weber, F., Rosenkranz, S., Castellán, J. P., Osborn, R., Hott, R., Heid, R., Bohnen, K. P., Egami, T., Said, A. H. & Reznik, D. Extended Phonon Collapse and the Origin of the Charge-Density Wave in  $2\text{H-NbSe}_2$ . *Physical Review Letters* **107**, 107403 (2011).
- 23 Leroux, M., Errea, I., Le Tacon, M., Souliou, S.-M., Garbarino, G., Cario, L., Bosak, A., Mauri, F., Calandra, M. & Rodière, P. Strong anharmonicity induces quantum melting of charge density wave in  $2\text{H-NbSe}_2$  under pressure. *Physical Review B* **92**, 140303 (2015).
- 24 Flicker, F. & van Wezel, J. Charge order from orbital-dependent coupling evidenced by  $\text{NbSe}_2$ . *Nat Commun* **6**, 7034 (2015).
- 25 Weber, F., Hott, R., Heid, R., Lev, L. L., Caputo, M., Schmitt, T. & Strocov, V. N. Three-dimensional Fermi surface of  $2\text{H-NbSe}_2$ : Implications for the mechanism of charge density waves. *Physical Review B* **97**, 235122 (2018).
- 26 Weber, F., Rosenkranz, S., Castellán, J. P., Osborn, R., Hott, R., Heid, R., Bohnen, K. P., Egami, T., Said, A. H. & Reznik, D. Extended Phonon Collapse and the Origin of the Charge-Density Wave in  $2\text{H-NbSe}_2$ . *Physical Review Letters* **107**, 107403 (2011).
- 27 Requardt, H., Lorenzo, J., Monceau, P., Currat, R. & Krisch, M. Dynamics in the charge-density-wave system  $\text{NbSe}_3$  using inelastic x-ray scattering with meV energy resolution. *Physical Review B* **66**, 214303 (2002).
- 28 Moncton, D. E., Axe, J. D. & DiSalvo, F. J. Neutron scattering study of the charge-density wave transitions in  $2\text{H-TaSe}_2$  and  $2\text{H-NbSe}_2$ . *Physical Review B* **16**, 801-819 (1977).
- 29 Kawano, H., Yoshizawa, H., Takeya, H. & Kadowaki, K. Anomalous phonon scattering below  $T_c$  in  $\text{YNi}_2^{11}\text{B}_2\text{C}$ . *Physical Review Letters* **77**, 4628-4631 (1996).
- 30 Stassis, C., Zarestky, J., Goldman, A., Canfield, P., Shirane, G. & Shapiro, S. Anomalous phonons below  $T_c$  in superconducting  $\text{RNi}_2\text{B}_2\text{C}$  (R=Lu,Y). *Physica C* **317-318**, 127-133 (1999).
- 31 Weber, F., Kreyssig, A., Pintschovius, L., Heid, R., Reichardt, W., Reznik, D., Stockert, O. & Hradil, K. Direct Observation of the Superconducting Gap in Phonon Spectra. *Physical Review Letters* **101**, 237002 (2008).
- 32 Weber, F., Rosenkranz, S., Pintschovius, L., Castellán, J. P., Osborn, R., Reichardt, W., Heid, R., Bohnen, K. P., Goremychkin, E. A., Kreyssig, A., Hradil, K. & Abernathy, D. L. Electron-Phonon Coupling in the Conventional Superconductor  $\text{YNi}_2\text{B}_2\text{C}$  at High Phonon Energies Studied by Time-of-Flight Neutron Spectroscopy. *Physical Review Letters* **109**, 057001 (2012).
- 33 Weber, F., Pintschovius, L., Reichardt, W., Heid, R., Bohnen, K. P., Kreyssig, A., Reznik, D. & Hradil, K. Phonons and electron-phonon coupling in  $\text{YNi}_2\text{B}_2\text{C}$ . *Physical Review B* **89**, 104503 (2014).
- 34 Kee, H.-Y. & Varma, C. M. Phonon anomalies induced by superconductivity. *Physical Review Letters* **79**, 4250-4253 (1997).
- 35 Kasinathan, D., Kuneš, J., Lazicki, A., Rosner, H., Yoo, C. S., Scalettar, R. T. & Pickett, W. E. Superconductivity and Lattice Instability in Compressed Lithium from Fermi Surface Hot Spots. *Physical Review Letters* **96**, 047004 (2006).
- 36 Allen, P. B., Kostur, V. N., Takesue, N. & Shirane, G. Neutron-scattering profile of  $\mathbf{Q} \neq 0$  phonons in BCS superconductors. *Physical Review B* **56**, 5552-5558 (1997).
- 37 Rhee, J. Y., Wang, X. & Harmon, B. N. Generalized susceptibility and magnetic ordering in rare-earth nickel boride carbides. *Physical Review B* **51**, 15585-15587 (1995).
- 38 Dugdale, S. B., Alam, M. A., Wilkinson, I., Hughes, R. J., Fisher, I. R., Canfield, P. C., Jarlborg, T. & Santi, G. Nesting properties and anisotropy of the Fermi surface of  $\text{LuNi}_2\text{B}_2\text{C}$ . *Physical Review Letters* **83**, 4824 (1999).

- 39 Baba, T., Yokoya, T., Tsuda, S., Watanabe, T., Nohara, M., Takagi, H., Oguchi, T. & Shin, S. Angle-resolved photoemission observation of the superconducting-gap minimum and its relation to the nesting vector in the phonon-mediated superconductor  $\text{YNi}_2\text{B}_2\text{C}$ . *Physical Review B* **81**, 180509 (2010).
- 40 Zarestky, J., Stassis, C., Goldman, A., Canfield, P. C., Shirane, C. & Shapiro, S. Phonon profiles in superconducting  $\text{YNi}_2\text{B}_2\text{C}$  and  $\text{LuNi}_2\text{B}_2\text{C}$ . *Physical Review B* **60**, 11932-11934 (1999).
- 41 Delaire, O., Ma, J., Marty, K., May, A. F., McGuire, M. A., Du, M. H., Singh, D. J., Podlesnyak, A., Ehlers, G., Lumsden, M. D. & Sales, B. C. Giant anharmonic phonon scattering in  $\text{PbTe}$ . *Nature Materials* **10**, 614-619 (2011).
- 42 Lanigan-Atkins, T., Yang, S., Niedziela, J. L., Bansal, D., May, A. F., Puretzy, A. A., Lin, J. Y. Y., Pajeroski, D. M., Hong, T., Chi, S., Ehlers, G. & Delaire, O. Extended anharmonic collapse of phonon dispersions in  $\text{SnS}$  and  $\text{SnSe}$ . *Nat Commun* **11**, 4430, doi:10.1038/s41467-020-18121-4 (2020).
- 43 Pickett, W. E. & Singh, D. J.  $\text{LuNi}_2\text{B}_2\text{C}$ : A novel Ni-based strong-coupling superconductor. *Physical Review Letters* **72**, 3702-3705 (1994).
- 44 Baba, T., Yokoya, T., Tsuda, S., Shin, S., Watanabe, T., Nohara, M., Takagi, H. & Oguchi, T. Fermi surface topology of borocarbide superconductor  $\text{YNi}_2\text{B}_2\text{C}$ : Angle-resolved photoemission spectroscopy. *Low Temperature Physics, Pts A and B* **850**, 683-684 (2006).
- 45 Starowicz, P., Liu, C., Khasanov, R., Kondo, T., Samolyuk, G., Gardenghi, D., Lee, Y., Ohta, T., Harmon, B., Canfield, P., Bud'ko, S., Rotenberg, E. & Kaminski, A. Direct observation of a Fermi surface and superconducting gap in  $\text{LuNi}_2\text{B}_2\text{C}$ . *Physical Review B* **77**, 134520 (2008).
- 46 Meyer, B., Elsässer, C., Lechermann, F. & Fähnle, M. *FORTRAN90 Program for Mixed-Basis Pseudopotential Calculations for Crystals* (Max-Planck-Institut für Metallforschung, Stuttgart).
- 47 Baroni, S., de Gironcoli, S., Dal Corso, A. & Giannozzi, P. Phonons and related crystal properties from density-functional perturbation theory. *Review of Modern Physics* **73**, 515-562 (2001).
- 48 Heid, R. & Bohnen, K.-P. Linear response in a density-functional mixed-basis approach. *Physical Review B* **60**, R3709-R3712 (1999).
- 49 Varma, C. M. & Weber, W. Phonon Dispersion in Transition Metals. *Physical Review Letters* **39**, 1094 (1977).
- 50 Doran, N. J. A calculation of the electronic response function in  $2\text{H-NbSe}_2$  including electron-phonon matrix element effects. *Journal of Physics C: Solid State Physics* **11**, L959 (1978).
- 51 Maschek, M., Rosenkranz, S., Heid, R., Said, A. H., Giraldo-Gallo, P., Fisher, I. R. & Weber, F. Wave-vector-dependent electron-phonon coupling and the charge-density-wave transition in  $\text{TbTe}_3$ . *Physical Review B* **91**, 235146 (2015).
- 52 Leroux, M., Le Tacon, M., Calandra, M., Cario, L. & al., e. Anharmonic suppression of charge density waves in  $2\text{H-NbS}_2$ . *Physical Review B* **86**, 155125 (2012).
- 53 Eiter, H.-M., Lavagnini, M., Hackl, R., Nowadnick, E. A., Kemper, A. F., Devereaux, T. P., Chu, J.-H., Analytis, J. G., Fisher, I. R. & Degiorgi, L. Alternative route to charge density wave formation in multiband systems. *Proceedings of the National Academy of Sciences* **110**, 64-69 (2013).
- 54 Soumyanarayanan, A., Yee, M. M., He, Y., van Wezel, J., Rahn, D. J., Rossmagel, K., Hudson, E. W., Norman, M. R. & Hoffman, J. E. Quantum phase transition from triangular to stripe charge order in  $\text{NbSe}_2$ . *Proceedings of the National Academy of Sciences* **110**, 1623-1627, doi:10.1073/pnas.1211387110 (2013).
- 55 Feng, Y., van Wezel, J., Wang, J., Flicker, F., Silevitch, D. M., Littlewood, P. B. & Rosenbaum, T. F. Itinerant density wave instabilities at classical and quantum critical points. *Nature Physics* **11**, 865-871 (2015).
- 56 Tsen, A. W., Hunt, B., Kim, Y. D., Yuan, Z. J., Jia, S., Cava, R. J., Hone, J., Kim, P., Dean, C. R. & Pasupathy, A. N. Nature of the quantum metal in a two-dimensional crystalline superconductor. *Nat Phys* **12**, 208-212 (2016).
- 57 Pekker, D. & Varma, C. M. Amplitude/Higgs Modes in Condensed Matter Physics. *Annual Review of Condensed Matter Physics* **6**, 269-297, doi:doi:10.1146/annurev-conmatphys-031214-014350 (2015).
- 58 Grasset, R., Cea, T., Gallais, Y., Cazayous, M., Sacuto, A., Cario, L., Benfatto, L. & Méasson, M.-A. Higgs-mode radiance and charge-density-wave order in  $2\text{H-NbSe}_2$ . *Physical Review B* **97**, 094502 (2018).
- 59 Zhu, X., Cao, Y., Zhang, J., Plummer, E. W. & Guo, J. Classification of charge density waves based on their nature. *Proceedings of the National Academy of Sciences* **112**, 2367-2371, doi:10.1073/pnas.1424791112 (2015).
- 60 Strocov, V. N., Wang, X., Shi, M., Kobayashi, M., Krempasky, J., Hess, C., Schmitt, T. & Patthey, L. Soft-X-ray ARPES facility at the ADDRESS beamline of the SLS: concepts, technical realisation and scientific applications. *Journal of Synchrotron Radiation* **21**, 32-44 (2014).
- 61 Strocov, V. N., Schmitt, T., Flechsig, U., Schmidt, T., Imhof, A., Chen, Q., Raabe, J., Betemps, R., Zimoch, D., Krempasky, J., Wang, X., Grioni, M., Piazzalunga, A. & Patthey, L. High-resolution soft X-ray beamline ADDRESS at the Swiss Light Source for resonant inelastic X-ray scattering and angle-resolved photoelectron spectroscopies. *Journal of Synchrotron Radiation* **17**, 631-643 (2010).
- 62 Braun, J., Minár, J., Mankovsky, S., Strocov, V. N., Brookes, N. B., Plucinski, L., Schneider, C. M., Fadley, C. S. & Ebert, H. Exploring the XPS limit in soft and hard x-ray angle-resolved photoemission using a temperature-dependent one-step theory. *Physical Review B* **88**, 205409 (2013).

## Figures

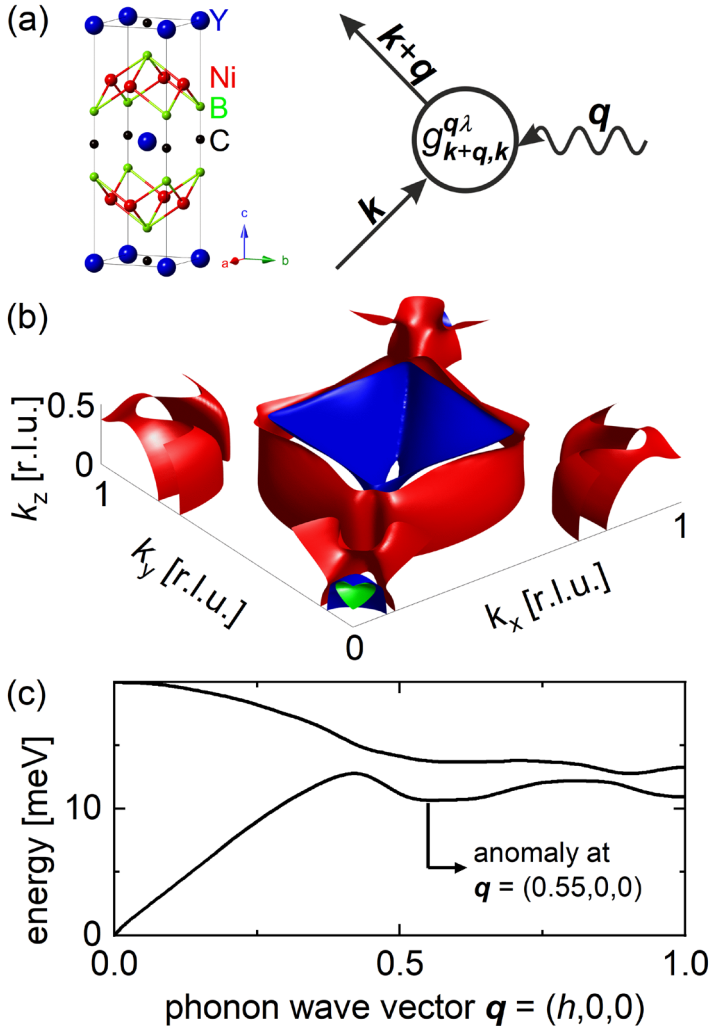


**Figure 1. Electron-phonon coupling**

(a) Crystal structure of  $\text{YNi}_2\text{B}_2\text{C}$  ( $I4/mmm$ ) and Feynman diagram of the EPC process including the EPC matrix element  $g_{k+q,k}^{q\lambda}$ . Wave vectors  $k$  and  $q$  refer to electron and phonon momentum space, respectively. (b) Calculated partial FS of  $\text{YNi}_2\text{B}_2\text{C}$ . Colors denote different bands crossing the Fermi energy. (c) Calculated phonon dispersion featuring an anomaly at  $q = (0.55, 0, 0)$ . Note nearly parallel sections of the Fermi surface at  $k_z = 0.5$  where 2D-eJDOS is enhanced.

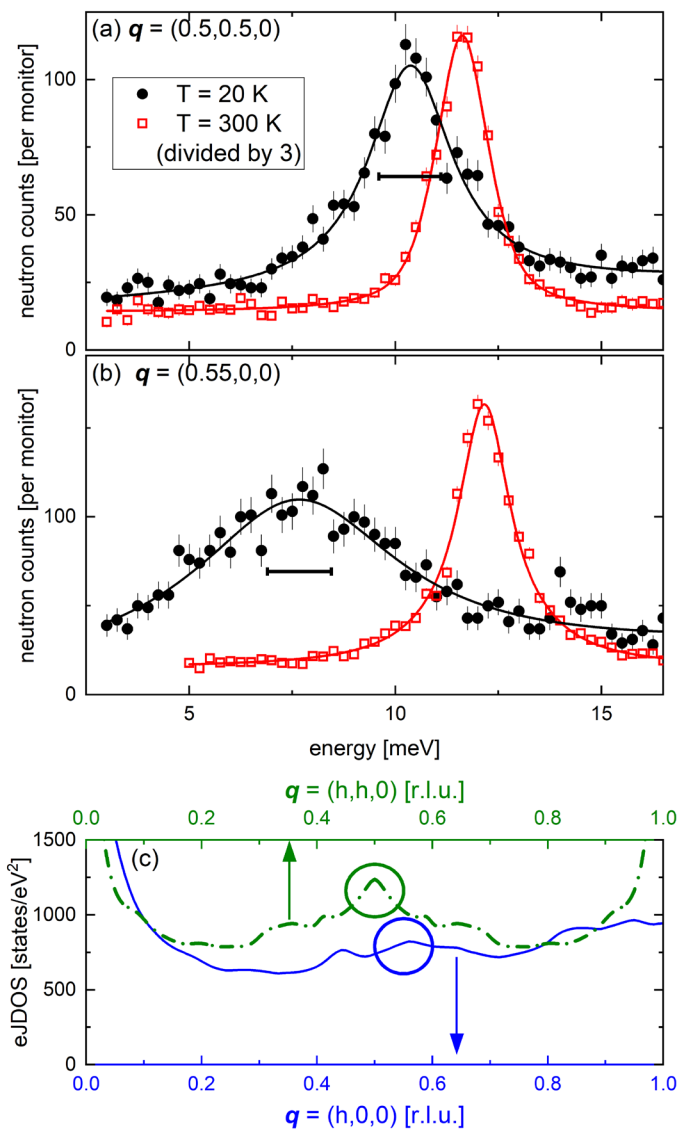


**Figure 2. Phonon broadening in YNi<sub>2</sub>B<sub>2</sub>C**

(a,b) Raw data from inelastic neutron scattering (INS) revealing the strong softening and broadening of c-axis polarized acoustic phonons at (a)  $Q = (0.5, 0.5, 7)$  and (b)  $Q = (0.45, 0, 7)$  corresponding to the reduced phonon wave vectors  $q = (0.5, 0.5, 0)$  and  $q = (0.55, 0, 0)$ , respectively, within the Brillouin zone adjacent to  $\tau = (1, 0, 7)$ . Horizontal bars indicate the full-width at half-maximum of the peak observed at  $T = 300$  K. (c) Calculated total electronic joint density-of-states (eJDOS) along  $\Gamma - X$  (solid blue line, bottom axis) and  $\Gamma - M - \Gamma$  (dashed green line, top axis) in  $q$  space. Circles indicate the phonon wave vectors corresponding to those shown in (a) and (b).

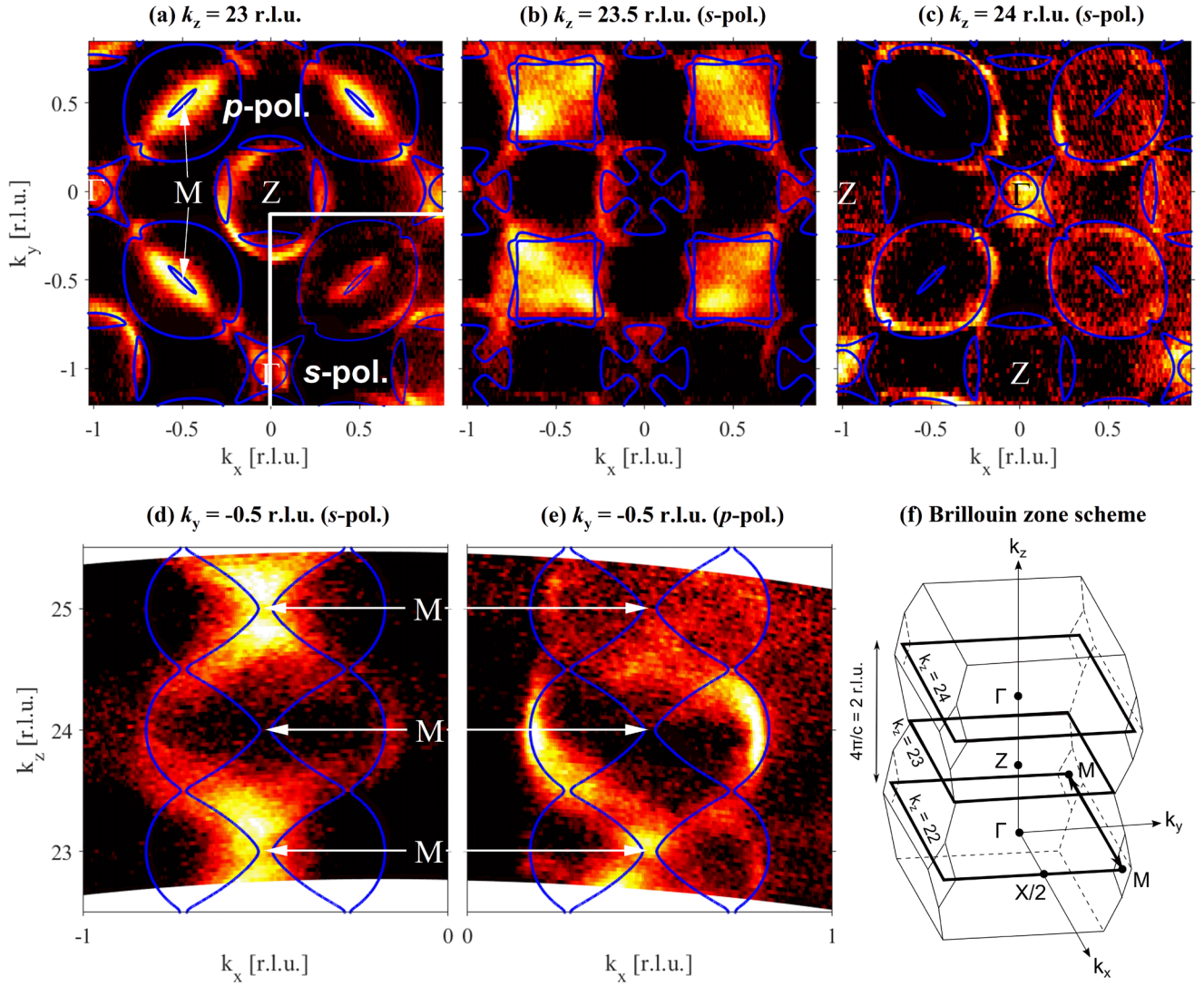


**Figure 3. Fermi surface from soft x-ray angle-resolved photoemission spectroscopy.**

Comparison of calculated Fermi surface (lines) and SX-ARPES intensities observed in the  $\Gamma - X/Z - M$  plane of the Brillouin zone (BZ) with (a)  $k_z = 23$  r.l.u. =  $13.7 \text{ \AA}^{-1}$  achieved at  $h\nu = 693$  eV, (b)  $23.5$  r.l.u. =  $14 \text{ \AA}^{-1}$  at  $725$  eV and (c)  $24$  r.l.u. =  $14.3 \text{ \AA}^{-1}$  at  $758$  eV. (d,e) Calculated Fermi surface (lines) and SX-ARPES intensities for the  $k_x - k_z$  plane at  $k_y = -0.5$  r.l.u.. Measurements shown in (a)-(d) were performed with  $p$  polarization except for the lower right quadrant in (a) which was obtained with  $s$  polarized light as data in (e). (f) Sketch of the BZ of  $\text{YNi}_2\text{B}_2\text{C}$ . Wave vectors are given in reciprocal lattice units (r.l.u.) of  $(2\pi/a, 2\pi/b, 2\pi/c)$  with  $a = b = 3.51 \text{ \AA}$  and  $c = 10.53 \text{ \AA}$ .

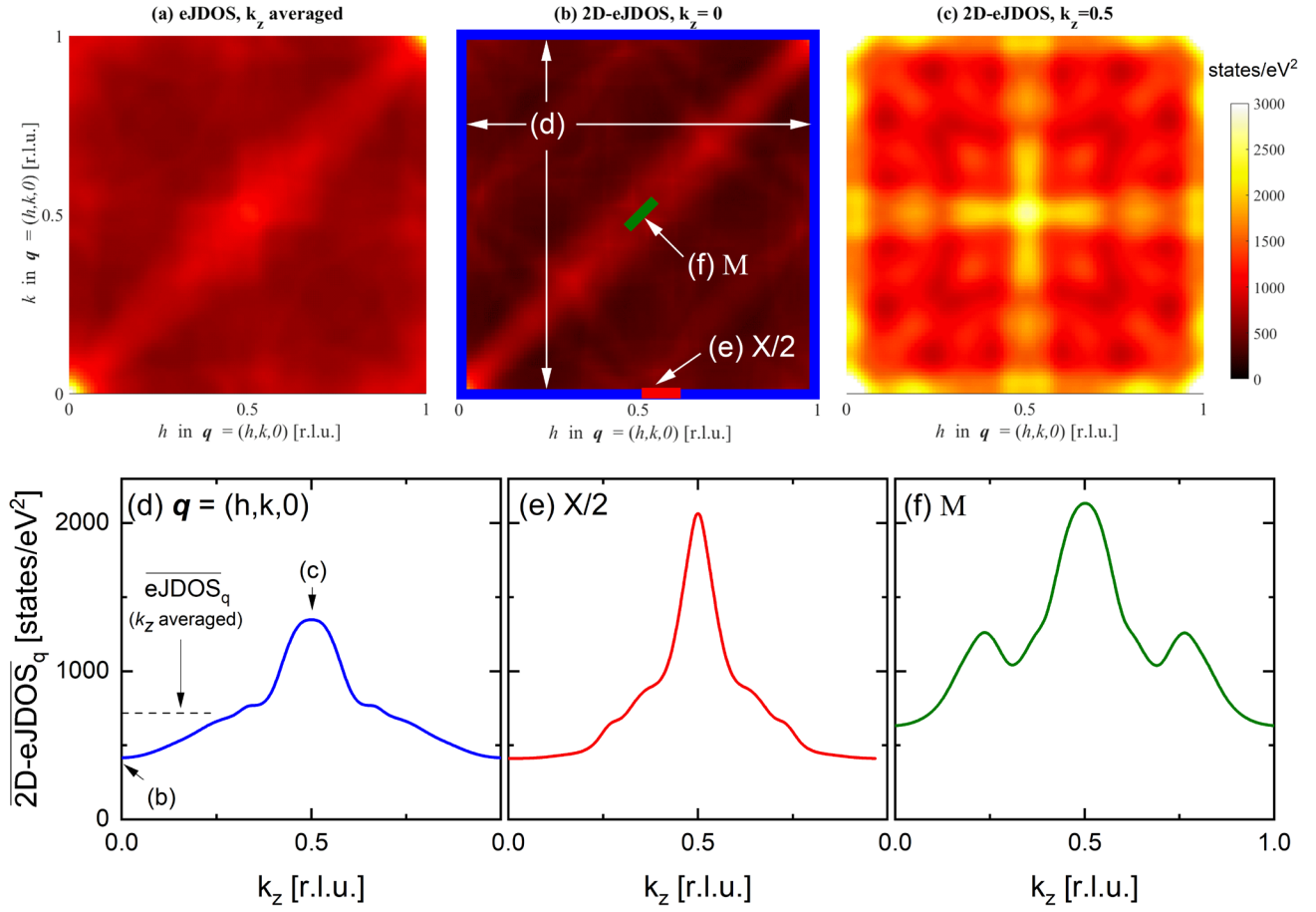


**Figure 4.  $k_z$ -dependence of electronic joint density-of-states (eJDOS).**

(a) eJDOS in the  $\mathbf{q} = (h, k, 0)$  plane with  $0 \leq h, k \leq 1$  r.l.u. averaged over the full 3D FS. (b,c) 2D-eJDOS( $k_z$ ) considering only the FS states with (b)  $k_z = 0$  and (c)  $k_z = 0.5$  r.l.u.. All results are given in states/eV<sup>2</sup> and the same color-code applies to (a)-(c). (d)-(f) Detailed  $k_z$  dependences of the  $\mathbf{q}$ -averaged 2D electronic joint density of states  $\overline{2D - eJDOS}_q$  averaged over three different ranges in  $\mathbf{q}$ : (d) full  $\mathbf{q} = (h, k, 0)$  plane [large blue square in (b)], (e)  $\mathbf{q} \approx X/2$  [red bar in (b)] and (f)  $\mathbf{q} = M$  [green bar in (b)], respectively. The black dashed horizontal line in (d) denotes the  $k_z$ -averaged value of  $\overline{eJDOS}_q$  deduced from the data shown in (a).

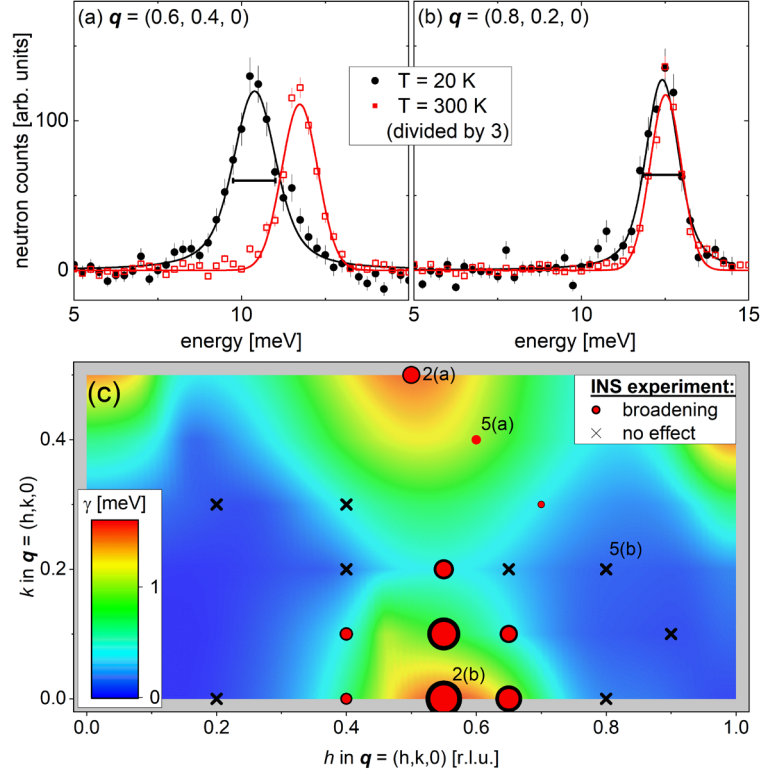


**Figure 5. Momentum dependent phonon broadening (DFPT+INS).**

(a,b) Raw data from inelastic neutron scattering (INS) demonstrating the momentum dependence of the softening and broadening of c-axis polarized acoustic phonons at (a)  $Q = (0.4, 0.4, 7)$  and (b)  $Q = (0.2, 0.2, 7)$  corresponding to the reduced phonon wave vectors  $q = (0.6, 0.4, 0)$  and  $q = (0.8, 0.2, 0)$ , respectively, within the Brillouin zone adjacent to  $\tau = (1, 0, 7)$ . Horizontal bars indicate the full-width at half-maximum of the peak observed at  $T = 300$  K. (c) Color-coded plot of the electronic contribution to the phonon linewidth  $\gamma_{EPC}^q$  for the transverse acoustic phonons investigated close to  $q = (0.5, 0.5, 0)$  [symbols at  $q = (0.5 + h, 0.5 - h, 0)$  and  $h = 0 - 0.4$ ] and  $q = (0.55, 0, 0)$  [other  $q$ ]. Red dots refer to wave vectors at which we observed phonon broadening. The symbol size scales relatively with the observed broadening. The symbols at  $q = (0.5, 0.5, 0)$  and  $(0.55, 0, 0)$  correspond to an additional Lorentzian broadening at  $T = 20$  K of 1.4 meV and 2.9 meV, respectively. Black crosses mark wave vectors where no phonon broadening was observed. Labels “2(a)”, “2(b)”, “5(a)” and “5(b)” refer to figures with corresponding data from INS.

## SUPPLEMENTARY INFORMATION TO:

### Electron-momentum dependence of electron-phonon coupling underlies dramatic phonon renormalization in $\text{YNi}_2\text{B}_2\text{C}$

Philipp Kurzhaus<sup>1</sup>, Geoffroy Kremer<sup>2</sup>, Thomas Jaouen<sup>2,3</sup>, Christopher W. Nicholson<sup>2</sup>, Rolf Heid<sup>1</sup>, Peter Nagel<sup>1</sup>, John-Paul Castellan<sup>1,4</sup>, Alexandre Ivanov<sup>5</sup>, Matthias Muntwiler<sup>6</sup>, Maxime Rumo<sup>2</sup>, Bjoern Salzmänn<sup>2</sup>, Vladimir N. Strocov<sup>6</sup>, Dmitry Reznik<sup>7,8</sup>, Claude Monney<sup>2</sup>, Frank Weber<sup>1,✉</sup>

<sup>1</sup> Institute for Quantum Materials and Technologies, Karlsruhe Institute of Technology, 76021 Karlsruhe, Germany

<sup>2</sup> Département de Physique and Fribourg Center for Nanomaterials, Université de Fribourg, 1700 Fribourg, Switzerland

<sup>3</sup> Univ Rennes, CNRS, IPR (Institut de Physique de Rennes) - UMR 6251, F-35000 Rennes, France

<sup>4</sup> Laboratoire Léon Brillouin (CEA-CNRS), CEA Saclay, F-91191 Gif-sur-Yvette, France

<sup>5</sup> Institut Laue-Langevin, 71 avenue des Martyrs CS 20156, 38042 Grenoble Cedex 9, France

<sup>6</sup> Paul Scherrer Institut, Swiss Light Source, 5232 Villigen PSI, Switzerland

<sup>7</sup> Department of Physics, University of Colorado at Boulder, Boulder, Colorado 80309, USA

<sup>8</sup> Center for Experiments on Quantum Materials, University of Colorado at Boulder, Boulder, Colorado 80309, USA

✉ [frank.weber@kit.edu](mailto:frank.weber@kit.edu)

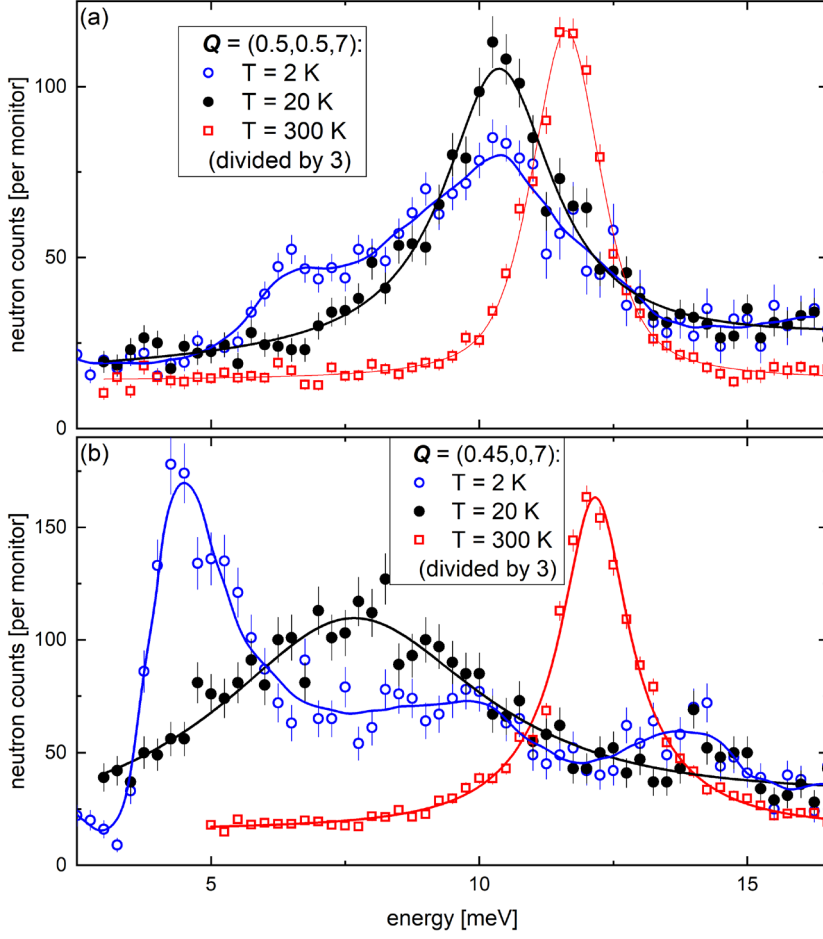


**FIG. S1.  $T_c$  effect in phonon spectroscopy.**

(a,b) Raw data from inelastic neutron scattering (INS) at (a)  $\mathbf{Q} = (0.5, 0.5, 7)$  and (b)  $\mathbf{Q} = (0.45, 0, 7)$  corresponding to the reduced phonon wave vectors  $\mathbf{q} = (0.5, 0.5, 0)$  and  $\mathbf{q} = (0.55, 0, 0)$ , respectively [as shown in Fig. 1(a,b)], along with data taken at  $T = 2$  K (blue circles), i.e. well below the superconducting transition temperature  $T_c = 15.2$  K. The blue lines are guides to the eye.

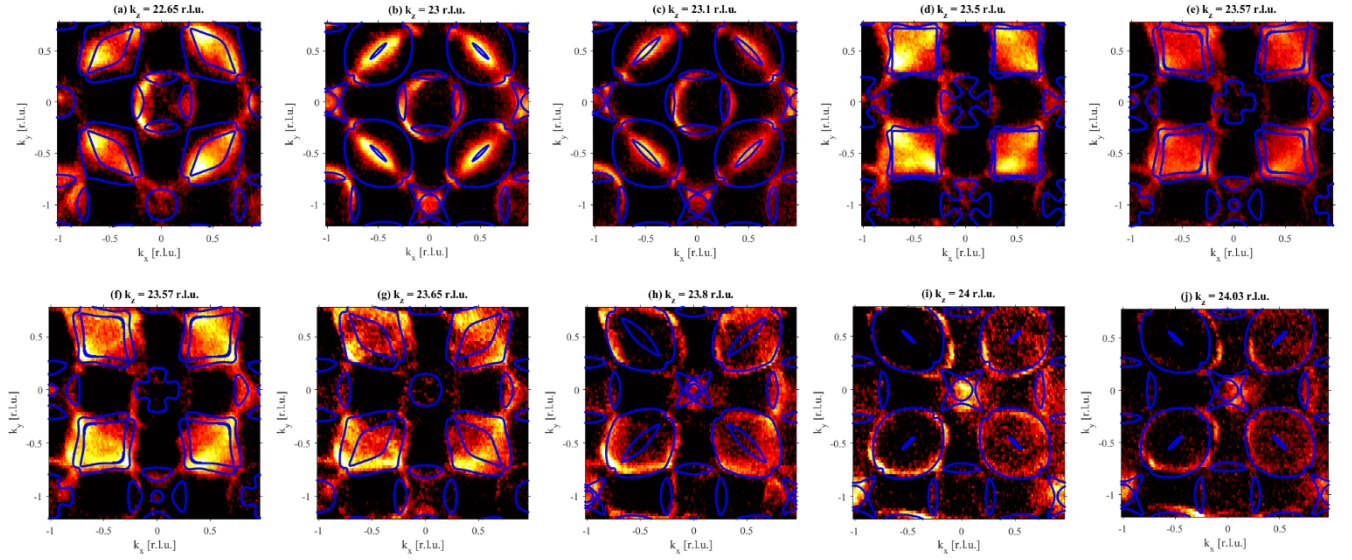


**FIG. S2. Fermi surface cuts at constant  $k_z$ .**

Comparison of calculated Fermi surface (lines) and SX-ARPES intensities observed in the  $\Gamma - X/Z - M$  plane for the given values of  $k_z$ . The data from (a)-(j) were obtained with incident energies of 670 eV, 693 eV, 700 eV, 725 eV, 730 eV, 730 eV, 735 eV, 745 eV, 758 eV and 760 eV, respectively.

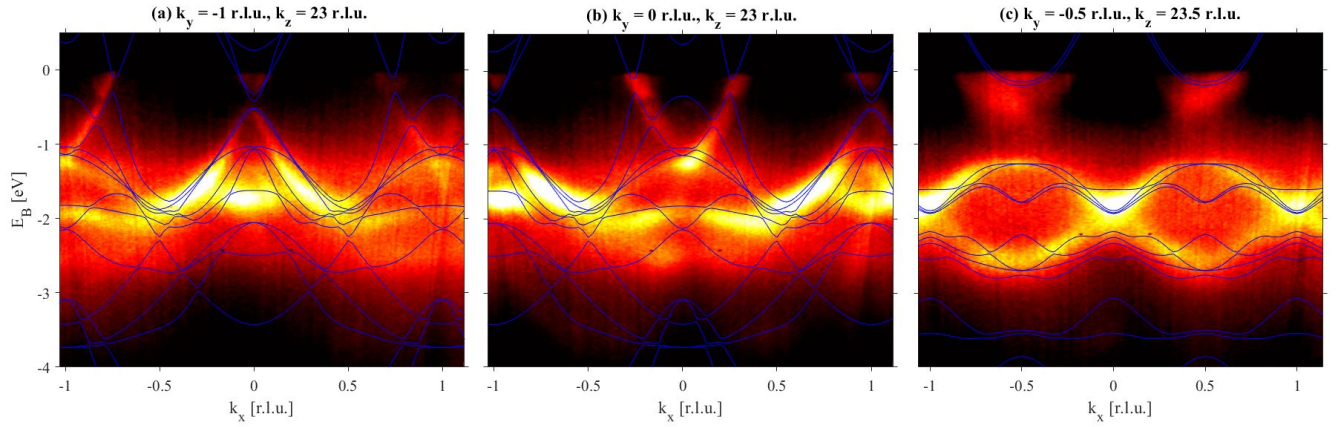


**FIG. S3. Band structure for constant  $k_y$  and  $k_z$ .**

Comparison of calculated band structure (lines) and SX-ARPES intensities for variable  $k_x$  at constant values of  $k_y$  and  $k_z$  given in the panel titles.

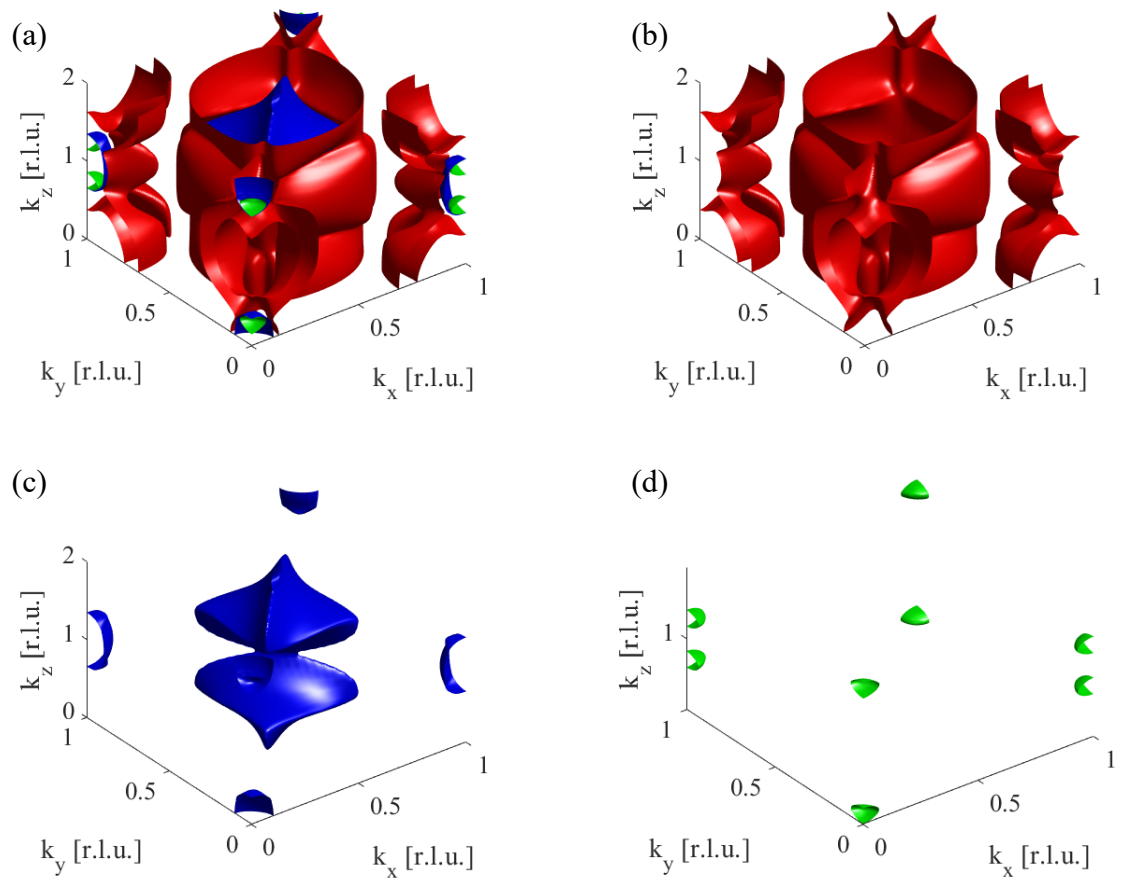


**FIG. S4. Calculated Fermi surface.**

(a) Complete calculated Fermi surface. (b)-(d) Fermi surfaces for the three different electronic bands.

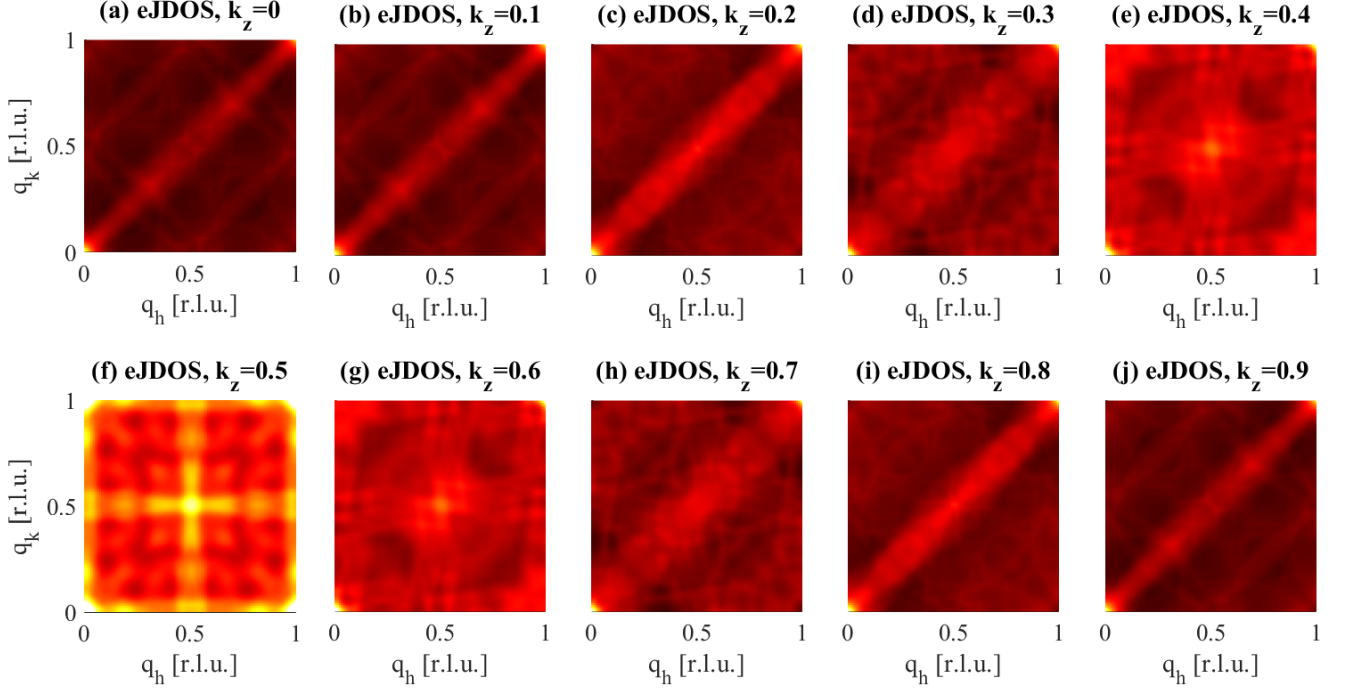


**FIG. S5.** Calculated electronic joint density-of-states (eJDOS) for fixed values of  $k_z = 0 - 0.9$  r.l.u.. The color scale is the same as for Fig. 3(b)(c).

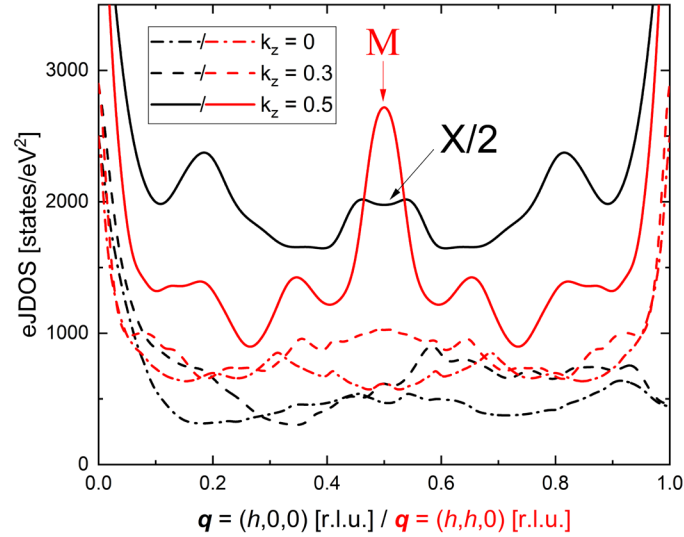


**FIG. S6.** Calculated electronic joint density-of-states (eJDOS) along two lines, i.e.,  $\mathbf{q} = (h, 0, 0)$  (black lines) and  $(h, h, 0)$  (red lines),  $h = 0 - 1$ , for fixed values of  $k_z = 0, 0.3, 0.5$ .

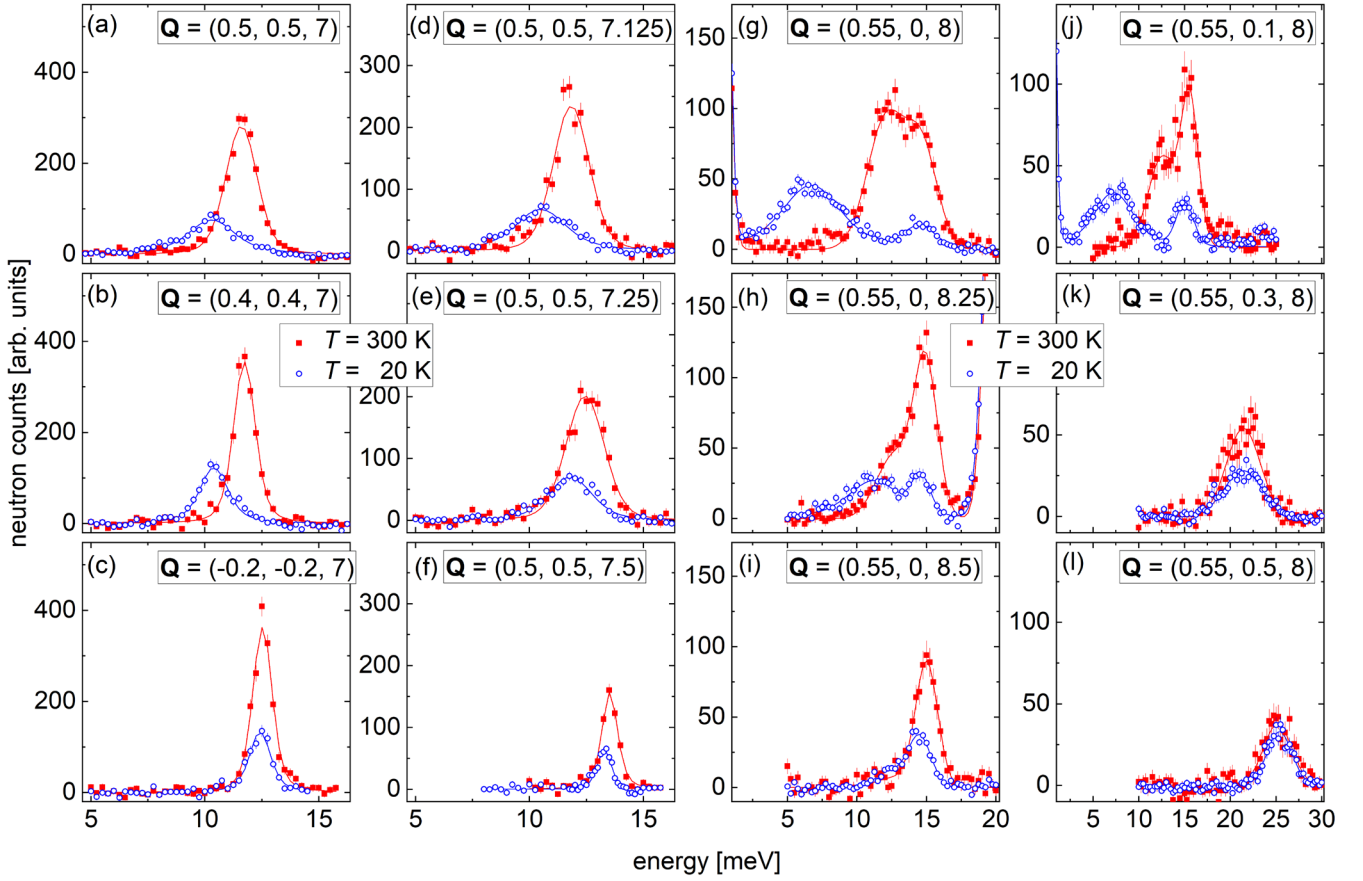


**FIG. S7. Phonon spectroscopy at wave vectors away from high-symmetry directions.**

Background subtracted scans in the vicinity of (a)-(f)  $\mathbf{Q} = (0.5, 0.5, 7)$  and (g)-(l)  $\mathbf{Q} = (0.55, 0, 8)$  at room temperature (red squares) and  $T = 20$  K (blue circles). The respective wave vector values are given in the legend of each panel. Note that  $\mathbf{Q} = (0.55, 0, 8)$  corresponds to the same reduced wave vector  $\mathbf{q} = (0.55, 0, 0)$  [with  $\boldsymbol{\tau} = (0, 0, 8)$ ] as  $\mathbf{Q} = (0.45, 0, 7)$  [with  $\boldsymbol{\tau} = (1, 0, 7)$ ]. Different to  $\mathbf{Q} = (0.45, 0, 7)$ , the first TO phonon has a finite structure factor at  $\mathbf{Q} = (0.55, 0, 8)$  and is clearly visible in agreement with our structure factor calculations. Hence, the phonon softening shown in (g) is the same as that in Fig. 1(b) – but measured on the neutron spectrometer *1T* located at LLB, CEA Saclay, France.

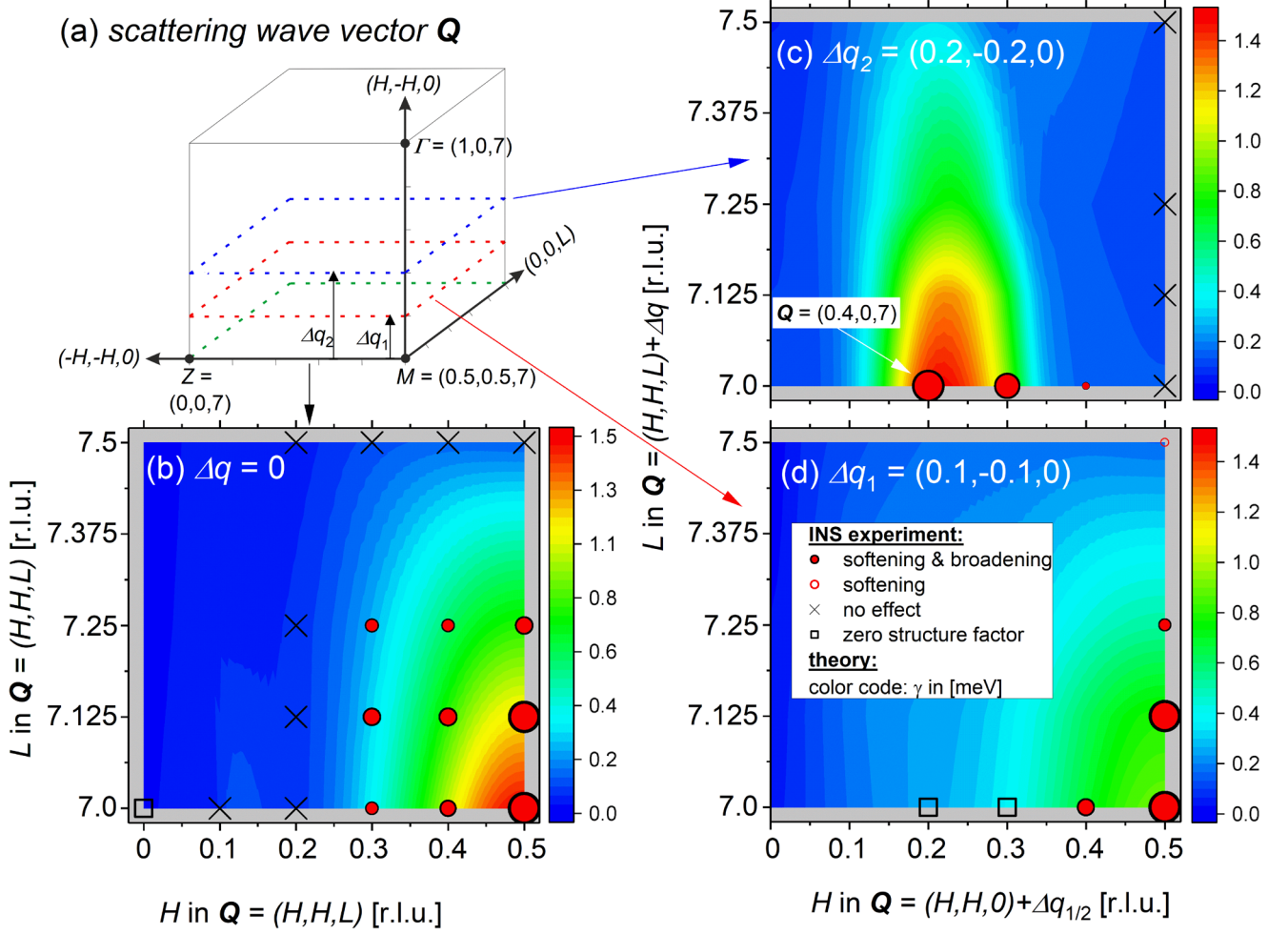


**FIG. S8. Momentum dependent phonon renormalization near  $\mathbf{Q} = (0.5, 0.5, 7)$ .**

(a) Illustration of the scattering geometry in the horizontal  $[110]$ - $[001]$  scattering plane. Measurements were also performed at out-of-plane wave vectors offset along the vertical  $[1, \bar{1}, 0]$  direction by  $\Delta\mathbf{q}_1 = (0.1, -0.1, 0)$  (red dashed plane) and  $\Delta\mathbf{q}_2 = (0.2, -0.2, 0)$  (blue dashed plane). The  $\Gamma$ ,  $Z$  and  $M$  points of the Brillouin zone are indicated (dots). (b)-(d) Color-coded plot of the calculated electronic contribution to the phonon linewidth  $\gamma$  for the transverse acoustic phonon mode investigated close to  $\mathbf{Q} = (0.5, 0.5, 7) + \Delta\mathbf{q}_{1/2}$ . Results are shown in the  $(H, H, L)$  scattering plane for (b)  $\Delta\mathbf{q} = 0$ , (c)  $\Delta\mathbf{q}_1 = (0.1, -0.1, 0)$  and (d)  $\Delta\mathbf{q}_2 = (0.2, -0.2, 0)$ . Symbols refer to results from INS measurements and indicate phonon renormalization as indicated in the legend of panel (d).  $\square$  (*zero structure factor*) indicates that the phonon intensity was too weak to be observed – in agreement with DFPT structure factor calculations. Size of symbols (dots, circles) scale with the strength of the phonon renormalization within each panel. The white arrow in (c) indicates  $\mathbf{Q} = (0.4, 0, 7)$  corresponding to a reduced wave vector  $\mathbf{q} = (0.6, 0, 0)$ .

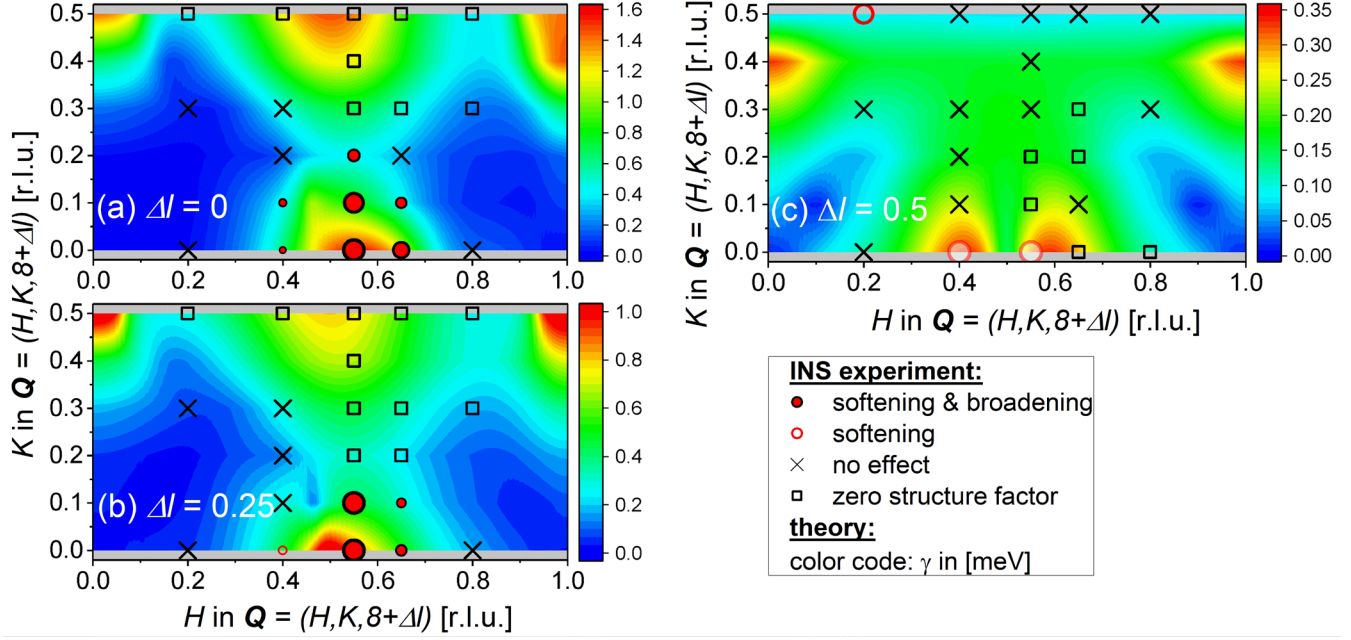


**FIG. S9. Momentum dependent phonon renormalization near  $\mathbf{Q} = (0.55, 0, 8)$ .**

Color-coded plot of the calculated electronic contribution to the phonon linewidth  $\gamma$  for the transverse acoustic phonon mode investigated close to  $\mathbf{Q} = (0.55, 0, 8 + \Delta l)$ . Results are shown in the  $(H, K)$  plane for (a)  $\Delta l = 0$ , (b) 0.25 r.l.u. and (c) 0.5 r.l.u.. Symbols refer to results from INS measurements and indicate phonon renormalization as indicated in the legend (lower right). Size of symbols (dots, circles) scale with the strength of the phonon renormalization within each panel.

## Supplemental Note 1:

### Opening of the superconducting gap $2\Delta$ observed in phonon spectroscopy

Below we explain in some more detail the superconductivity-induced changes of the phonon line shape observed for the TA phonon modes in  $\text{YNi}_2\text{B}_2\text{C}$  both at  $\mathbf{q} = (0.5, 0.5, 0)$  [Fig. S1(a)] and  $\mathbf{q} = (0.55, 0, 0)$  [Fig. S1(b)]. Previously, some of us reported on this phenomenon in Ref. <sup>1</sup>. Similar studies for other superconductors can be found in Refs. <sup>2-4</sup>.

Figure S1(a) shows the evolution through  $T_c = 15.2$  K of the low temperature line shape of the TA phonon mode at the M point. On cooling from  $T = 300$  K to 20 K, this phonon softens and broadens substantially, indicative of a strong EPC [see temperature dependences given in Figs. 1(c) and S1(c)]. However, the line shape remains Lorentzian to a very good approximation. On further cooling through  $T_c$ , the line shape starts to deviate strongly from a Lorentzian. In particular, a step-like increase at a certain energy  $E_s \approx 5.7$  meV appears in the spectrum taken at  $T = 2$  K [Fig. S1(a)]. According to the theory developed by Allen et al. <sup>5</sup>, a part of the low energy tail which lies below the value of the superconducting gap  $2\Delta$  is pushed up in energy to form a narrow spike at  $2\Delta$ . The theory is based on the full quantum mechanical treatment of EPC where vibrational and electronic excitations mix into hybrid modes. The finite spectrometer resolution should wash out the theoretically predicted spike in experiments resulting in a sharp intensity increase at  $2\Delta$ . The predicted intensity increase corresponds to the one we observe at  $E_s$ , i.e.  $2\Delta(T=2\text{K}) = 5.7$  meV for the TA phonon at  $\mathbf{q} = (0.5, 0.5, 0)$ . In Ref. <sup>1</sup>, we were able to employ this signature of the superconducting gap in phonon spectroscopy in order to carefully determine the temperature dependence of  $2\Delta$ .

The phonon at  $\mathbf{q} = (0.55, 0, 0)$  [Fig. S1(b)] has a significantly lower energy than the M point phonon discussed above [see Fig. 1(c)] and, moreover, has a much larger linewidth [Fig. S1(c)]. As a consequence, the superconductivity-induced redistribution of spectral weight is even stronger, but the superconducting gap cannot be inferred from the data as easily, except for temperatures close to  $T_c$  where the gap is still small. For lower temperatures, most of the spectral weight condenses into a fairly sharp peak [Fig. S1(b)] whose energy is – according to theory – somewhat below  $2\Delta$ . According to Ref. <sup>5</sup>, this resonance can be regarded as a mixed vibrational or superelectronic collective excitation. Its position with respect to  $2\Delta$  has to be determined from calculations for the parameter values of this particular phonon. Again, the theory reproduces the observed line shapes sufficiently well to precisely determine the gap value.

For the current subject regarding the phonon renormalization in the normal state of  $\text{YNi}_2\text{B}_2\text{C}$ , the superconductivity-induced changes of the phonon line shape are important. They demonstrate that the linewidth at low temperatures of  $T \approx 20$  K is sensitive to changes of the electronic states at the FS and, thus, EPC in nature and not related to anharmonic broadening as observed in  $2H\text{-NbSe}_2$  <sup>6</sup>.

## Supplemental Note 2:

### Momentum dependent phonon renormalization

Phonon spectroscopy with INS is done at absolute wave vectors  $\mathbf{Q} = \boldsymbol{\tau} + \mathbf{q}$ , where  $\boldsymbol{\tau}$  denotes the center of a Brillouin zone (BZ) and  $\mathbf{q}$  is the reduced wave vector within this BZ. Phonon energies and linewidths are defined within the first Brillouin zone (BZ) and, thus, do not depend on  $\boldsymbol{\tau}$ . In contrast, the phonon intensity varies strongly with  $\boldsymbol{\tau}$ . For example, the TA mode at the  $M$  point discussed in our work has a large intensity at  $\mathbf{Q} = (0.5, 0.5, 7)$  [Fig. 1(a)] but cannot be observed at  $(0.5, 0.5, L)$  with  $L = 2, 4, 6$ .<sup>7</sup> We note that the accurate determination of phonon linewidths requires sizeable intensities. Thus, we could only evaluate the temperature dependence of the phonon energy in some cases with weak scattering intensities. In other cases, even this was not possible anymore.

In Figure 4 of the main manuscript we show results only in reduced wave vectors  $\mathbf{q} = (h, k, 0)$  for the sake of clear assignments. The full momentum dependent investigation, however, can only be presented in absolute wave vectors and is shown in Figures S7 – S9 discussed below.

Background subtracted INS data are shown in Figure S7. Measurements around the  $M$ -point were done at the IN8 triple-axis spectrometer, ILL, with Cu200 monochromator and Cu200 analyzer in order to achieve the best energy resolution. A fixed final energy of 14.7 meV was used and the sample was aligned in the horizontal 110-001 scattering plane. The data [Figs. S7(a)-(f)] visualize the phonon renormalization by cooling from room temperature (red dots) to 20 K (blue circles). Data at different positions along the [110] [Figs. S7(a)-(c)] and [001] directions [Figs. S7(d)-(f)] emphasize the evolution of the phonon softening and broadening which decrease moving away from the  $M$  point.

In addition to measurements within the horizontal 110-001 scattering plane, we performed scans also at out-of-plane wave vectors which were offset along the vertical  $[1\bar{1}0]$  direction by  $\Delta\mathbf{q}_1 = (0.1, -0.1, 0)$  and  $\Delta\mathbf{q}_2 = (0.2, -0.2, 0)$ . The scattering geometry is depicted in Fig. S8(a), where the horizontal 110-001 scattering plane as well as those offset by  $\Delta\mathbf{q}_1$  and  $\Delta\mathbf{q}_2$  are indicated by green (bottom), red (middle) and blue dashed lines (top). The corresponding results for the main scattering plane are shown in panel (b). In contrast to Fig. 4(b), results in Fig. S8(b) are given in absolute wave vectors with the  $M$  point located in the lower right corner at  $\mathbf{Q} = (0.5, 0.5, 7)$ . We emphasize that the center of the BZ – corresponding to the  $M$  point at  $\mathbf{Q} = (0.5, 0.5, 7)$  is  $\boldsymbol{\tau} = (1, 0, 7)$  [see  $\Gamma$  point in Fig. S8(a)]. Hence, the line  $\mathbf{Q} = (H, H, 7)$  [horizontal line in bottom of Fig. S8(b)] corresponds to  $\mathbf{q} = (0.5+h, 0.5-h, 0)$  with  $h = 0 - 0.4$ . The latter are the points given also in Fig. 4(a). We did not include more points in Fig. 4(a), since the assignment in units of the reduced wave vector  $\mathbf{q}$  would have been unclear with regard to measurements done in the BZ adjacent to  $\boldsymbol{\tau} = (0, 0, 8)$  which are discussed below.

The detailed momentum dependence of the experimentally observed phonon renormalization is in good agreement with the predicted momentum dependence of the electronic contribution to the phonon linewidth  $\gamma$ , where the symbol size in Fig. S8(b) scales with the strength of the observed effects. Panels (c) and (d) show the analogue results but for wave vectors offset by (c)  $\Delta\mathbf{q}_2 = (0.2, -0.2, 0)$  and (d)  $\Delta\mathbf{q}_1 = (0.1, -0.1, 0)$ . There is a clear shift of the phonon renormalization. In the main scattering plane [Fig. S8(b)] and the one offset by  $\Delta\mathbf{q}_1$  [Fig. S8(d)] the effects are strongest at  $H = 0.5$  [lower left corner in (b) and (d)], whereas the maximum effect for  $\Delta\mathbf{q}_2$  occurs at  $H = 0.2$  [Fig. S8(c)]. Here, we note that  $H = 0.2$  corresponds in the notation of Fig. S8 to  $\mathbf{Q} = (0.2, 0.2, 7) + (0.2, -0.2, 0) = (0.4, 0, 7)$  and, thus, to  $\mathbf{q} = \mathbf{Q} - \boldsymbol{\tau} = (0.4, 0, 7) - (1, 0, 7) = (-0.6, 0, 0)$ . Hence, results with offset  $\Delta\mathbf{q}_2$  are

actually very close to the anomaly along the [100] direction on which we focused in our measurements taken close to  $\mathbf{Q} = (0.55, 0, 8)$ . However, we note that we used the very good energy resolution at the IN8 spectrometer to investigate the temperature dependence of the anomaly at  $\mathbf{q} = (0.55, 0, 0)$  at an absolute wave vector of  $\mathbf{Q} = (0.45, 0, 7)$ . Corresponding results are shown in Fig. 1(b).

We investigated the momentum dependence of the phonon anomaly centered at  $\mathbf{q} = (0.55, 0, 0)$  more extensively in the BZ adjacent to  $\boldsymbol{\tau} = (0, 0, 8)$ . We note that the bulk of the previous data for anomalous phonon scattering in  $\text{YNi}_2\text{B}_2\text{C}$  has been obtained at  $\mathbf{Q} = (h, 0, 8)$ ,  $0 \leq h \leq 1$ <sup>1,7-9</sup>.

Corresponding background subtracted INS data are shown in Figure S7(g)-(l). Measurements close to the anomaly at  $\mathbf{Q} = (0.55, 0, 8)$  were done at the 1T triple-axis spectrometer, LLB, with PG002 monochromator and PG002 analyzer. A fixed final energy of 14.7 meV was used and the sample was aligned in the horizontal 100-001 scattering plane. The data [Figs. S7(g)-(l)] visualize the phonon renormalization by cooling from room temperature (red dots) to 20 K (blue circles). Data at different positions along the [001] [Figs. S7(g)-(i)] and the out-of-plane [010] directions [Figs. S7(j)-(l)] emphasize the evolution of the phonon softening and broadening which decrease moving away from  $\mathbf{Q} = (0.55, 0, 8)$ . The data also show the presence of higher energy phonon modes, e.g. an optic mode with an energy of 13-14 meV at  $\mathbf{Q} = (0.55, 0, 8)$ , the center of the anomaly in the TA mode [Fig. S7(g)]. This optic mode does not change with temperature as was already reported in previous work<sup>7</sup>.

Results for the momentum dependent phonon renormalization observed in the BZ adjacent to  $\boldsymbol{\tau} = (0, 0, 8)$  are summarized in Figure S9 for offsets in the  $l$  component of (a) 0, (b) 0.25 r.l.u. and (c) 0.5 r.l.u. from the zone center value. Again we find that the regions in reciprocal space with large calculated values of  $\gamma$  agree well with the points at which we observe detectable phonon renormalization. We emphasize that the fact that we did not observe phonon renormalization at some wave vectors for which large  $\gamma$  values are calculated, e.g. at the  $M$  point [ $\mathbf{Q} = (0.5, 0.5, 8)$  in Fig. S9(a)], is solely due to a vanishing phonon structure factor of the TA mode at the  $M$  point in this BZ (marked by open square symbols) in agreement with calculations for the structure factor.

## SM – references:

- 1 Weber, F., Kreyssig, A., Pintschovius, L., Heid, R., Reichardt, W., Reznik, D., Stockert, O. & Hradil, K. Direct Observation of the Superconducting Gap in Phonon Spectra. *Physical Review Letters* **101**, 237002 (2008).
- 2 Weber, F. & Pintschovius, L. Superconductivity-induced distortions of phonon lineshapes in niobium. *Physical Review B* **82**, 024509 (2010).
- 3 Weber, F., Rosenkranz, S., Heid, R. & Said, A. H. Superconducting energy gap of  $2\text{H-NbSe}_2$  in phonon spectroscopy. *Physical Review B* **94**, 140504(R) (2016).
- 4 Sauer, A., Zocco, D. A., Said, A. H., Heid, R., Böhmer, A. & Weber, F. Electron-phonon coupling and superconductivity-induced distortion of the phonon lineshape in  $\text{V}_3\text{Si}$ . *Physical Review B* **99**, 134511 (2019).
- 5 Allen, P. B., Kostur, V. N., Takesue, N. & Shirane, G. Neutron-scattering profile of  $\mathbf{Q} \neq 0$  phonons in BCS superconductors. *Physical Review B* **56**, 5552-5558 (1997).
- 6 Leroux, M., Errea, I., Le Tacon, M., Souliou, S.-M., Garbarino, G., Cario, L., Bosak, A., Mauri, F., Calandra, M. & Rodière, P. Strong anharmonicity induces quantum melting of charge density wave in  $2\text{H-NbSe}_2$  under pressure. *Physical Review B* **92**, 140303 (2015).
- 7 Weber, F., Pintschovius, L., Reichardt, W., Heid, R., Bohnen, K. P., Kreyssig, A., Reznik, D. & Hradil, K. Phonons and electron-phonon coupling in  $\text{YNi}_2\text{B}_2\text{C}$ . *Physical Review B* **89**, 104503 (2014).
- 8 Kawano, H., Yoshizawa, H., Takeya, H. & Kadowaki, K. Anomalous phonon scattering below  $T_c$  in  $\text{YNi}_2^{11}\text{B}_2\text{C}$ . *Physical Review Letters* **77**, 4628-4631 (1996).
- 9 Zarestky, J., Stassis, C., Goldman, A., Canfield, P. C., Shirane, C. & Shapiro, S. Phonon profiles in superconducting  $\text{YNi}_2\text{B}_2\text{C}$  and  $\text{LuNi}_2\text{B}_2\text{C}$ . *Physical Review B* **60**, 11932-11934 (1999).